Article

Increased enhancer–promoter interactions during developmental enhancer activation in mammals

Zhuoxin Chen ⬚[1], Valentina Snetkova ⬚[2], Grace Bower[1], Sandra Jacinto[1], Benjamin Clock ⬚[1], Atrin Dizehchi[1], Iros Barozzi ⬚[2,8], Brandon J. Mannion ⬚[2,3], Ana Alcaina-Caro ⬚[4], Javier Lopez-Rios ⬚[4,5], Diane E. Dickel[2,9], Axel Visel ⬚[2,6,7], Len A. Pennacchio ⬚[2,3,6] & Evgeny Z. Kvon ⬚[1]✉

Remote enhancers are thought to interact with their target promoters via physical proximity, yet the importance of this proximity for enhancer function remains unclear. Here we investigate the three-dimensional (3D) conformation of enhancers during mammalian development by generating high-resolution tissue-resolved contact maps for nearly a thousand enhancers with characterized in vivo activities in ten murine embryonic tissues. Sixty-one percent of developmental enhancers bypass their neighboring genes, which are often marked by promoter CpG methylation. The majority of enhancers display tissue-specific 3D conformations, and both enhancer–promoter and enhancer–enhancer interactions are moderately but consistently increased upon enhancer activation in vivo. Less than 14% of enhancer–promoter interactions form stably across tissues; however, these invariant interactions form in the absence of the enhancer and are likely mediated by adjacent CTCF binding. Our results highlight the general importance of enhancer–promoter physical proximity for developmental gene activation in mammals.

Enhancers, or *cis*-regulatory elements, ensure precise spatiotemporal control of gene expression during development. This process is mediated by transcription factors and co-activators, which relay regulatory information from enhancers to their target promoters across distances that can exceed 1 Mb[1–4]. This enhancer–promoter (E–P) communication is thought to occur within so-called topologically associated domains (TADs), fundamental organizational units of the genome formed through the process of loop extrusion by cohesin and CCCTC-binding factor (CTCF)[5–7]. Disruption of TADs or intra-TAD

chromatin interactions can cause erroneous downregulation of gene expression or gene activation and can lead to human disease, indicating the importance of proper E–P communication for gene activation[8–10].

Remote enhancers are thought to communicate with their target genes via physical proximity established by chromatin looping[5,11–13]. However, whether physical proximity is linked to enhancer function remains unclear. One model suggests that E–P contacts are formed only during gene activation. Indeed, the establishment of E–P interactions at many genetic loci occurs coordinately with gene transcription[14–17].

[1]Department of Developmental and Cell Biology, School of the Biological Sciences, University of California, Irvine, CA, USA. [2]Environmental Genomics and Systems Biology Division, Lawrence Berkeley National Laboratory, Berkeley, CA, USA. [3]Comparative Biochemistry Program, University of California, Berkeley, CA, USA. [4]Centro Andaluz de Biología del Desarrollo, CSIC, Universidad Pablo de Olavide, Junta de Andalucía, Seville, Spain. [5]School of Health Sciences, Universidad Loyola Andalucía, Seville, Spain. [6]U.S. Department of Energy Joint Genome Institute, Walnut Creek, CA, USA. [7]School of Natural Sciences, University of California, Merced, CA, USA. [8]Present address: Center for Cancer Research, Medical University of Vienna, Vienna, Austria. [9]Present address: Octant, Inc, Emeryville, CA, USA. ✉e-mail: ekvon@uci.edu

In line with this, artificial tethering of an enhancer to the developmentally silenced β-globin promoter results in ectopic gene activation[18], suggesting a potentially instructive role of chromatin looping in E–P communication and gene activation. An alternative model is that E–P contacts are stable and/or preformed and thus not temporally linked to gene activation. For example, mouse limb enhancers at *Hoxd* and *Shh* loci, human fibroblast and keratinocyte enhancers and many early *Drosophila* enhancers appear to form E–P chromatin loops even when the genes are not expressed[17,19–22]. In a third model, there is no association between gene activation and E–P physical proximity[23], and, in some cases, an increase in E–P distance is observed upon gene activation, challenging a simple looping model[24,25]. While all these models exist in principle, the predominant mode of activation for bona fide developmental enhancers remains unclear, as past research has focused on well-studied genetic loci or enhancers defined based on the presence of open chromatin, co-activators, enhancer RNA or enhancer-associated histone modifications, thus making it challenging to separate functional E–P interactions from other types of chromatin interactions[26].

To better understand E–P interactions during mammalian development, we used a unique resource of experimentally verified human and mouse enhancers[27]. Many of these enhancers have been shown to be critical for developmental and disease processes[8,28–32]. However, the 3D nuclear organization of these loci remains largely uncharacterized. We thus generated high-resolution enhancer interactome maps across ten mouse embryonic tissues for 935 bona fide developmental enhancers with characterized in vivo activity at mid-gestation. We identified thousands of enhancer contacts and found that most enhancer loci display tissue-specific 3D conformations. Moreover, developmental enhancers display higher interaction frequencies with promoters and neighboring enhancers in tissues where they are active. We also show that invariant E–P interactions are less prevalent and likely form independently of enhancer activity. Sixty-one percent of developmental enhancers skip their immediate neighboring genes, which are often marked by promoter DNA methylation. Our results provide a global view of tissue-specific enhancer 3D chromatin conformation and support the broad importance of E–P physical proximity for developmental gene activation.

Results

Enhancer interactome for 935 developmental enhancers across ten embryonic tissues

To create a map of in vivo enhancer-centric chromatin interactions in developing mouse embryos, we used the VISTA Enhancer Browser, a unique resource of human and mouse enhancers with in vivo activities experimentally validated in transgenic mice[27]. This resource verifies and thus allows direct comparison of tissue and cell types in which each tested enhancer is active or inactive. We created a sizable and robust core set of experimentally verified in vivo enhancers comprising 935 enhancers with highly reproducible activities in mouse embryonic tissues at mid-gestation (embryonic day (E)11.5). Tissues in which enhancers were active included the forebrain, midbrain, hindbrain, neural tube, craniofacial structures, limb buds, heart and other tissues and cell types (Supplementary Table 1). To assess tissue-specific chromatin interactions centered on these enhancers, we collected ten tissues from E11.5 mouse embryos (forebrain, midbrain, hindbrain, neural tube, face, forelimb, hindlimb, heart, tail and trunk) with two biological replicates per tissue and performed enhancer capture Hi-C (Fig. 1a and the Methods). This diverse tissue panel represents all major embryonic organs in which the selected enhancers are active and for which extensive chromatin state maps were created as part of the ENCODE project[33]. We designed RNA probes (Agilent SureSelect platform) targeting each of the 935 enhancers as well as 176 promoters and 87 elements with no reproducible enhancer activity at E11.5 as negative controls (Fig. 1a, Methods and Supplementary Table 1).

After restriction fragment pooling and quality control, we identified a total of 24,657 significant interactions across all tissues, 17,988 of which were baited on enhancers. Approximately 80% of enhancer-centric interactions were called within the same TAD (Extended Data Fig. 1a–d, Supplementary Table 2 and the Methods). These interactions included E–P (2,818), enhancer–enhancer (E–E) (5,612), enhancer–CTCF (5,140) and other types of contacts (Extended Data Fig. 1d). Most enhancers only interacted with one or two genes with a median distance between an enhancer and a target promoter of ~410 kb (Fig. 1c and Extended Data Fig. 1f). For example, in the midbrain, the hs654 enhancer displayed the strongest significant interaction with promoters of two adjacent genes, *Zic1* and *Zic4*, located ~600 kb away. Reciprocally, the viewpoint containing the *Zic1* and *Zic4* promoters (located ~3 kb from each other) also showed significant interaction with the hs654 enhancer (Fig. 1b).

To provide orthogonal support for the functional relevance of identified chromatin interactions, we compared them with ENCODE chromatin data that were generated for an overlapping set of tissues from E11.5 mouse embryos. We found that the 935 in vivo positive enhancers and 176 promoters contacted other elements annotated by ENCODE (promoters, enhancers, CTCF sites) significantly more often than the negative 87 control regions, thus supporting the enhancer interactions identified above (Extended Data Fig. 1g,h).

We also identified significant tissue-specific chromatin interactions between enhancers overlapping mutations implicated in human congenital disorders and their putative target genes in relevant tissues. These examples included previously characterized enhancers involved in congenital malformations and autism as well as enhancer variants identified in patients with neurodevelopmental disorders with previously unknown regulatory targets (Fig. 1d,e, Extended Data Fig. 2 and Supplementary Table 3). These results provide additional evidence for the specific regulatory connection between disease-associated enhancers and their in vivo target genes and further support E–P chromatin interactions identified by capture Hi-C.

Most enhancers bypass adjacent genes, which are often methylated

Nearly 61% of enhancers in our study did not interact with the promoters of adjacent genes but instead contacted more distal genes (Fig. 2a). For example, the hs271 forebrain enhancer strongly interacts with the promoter of *Nr2f1* located ~650 kb away but does not form any significant interactions with the more proximally located *Pou5f2* promoter (Fig. 2b,c). Similarly, a cluster of three forebrain enhancers, hs267, hs266 and hs853, interacted with the *Mir9-2* promoter located ~800 kb away, skipping over the more proximal *Tmem161b* promoter (Extended Data Fig. 3a).

All skipped genes could be divided into two categories based on their epigenetic status (Fig. 2d and Extended Data Fig. 4). For example, in the forebrain, 52.4% of skipped genes were methylated and not accessible at their promoters (80.8% average CpG methylation at transcription start sites (TSSs); eightfold lower DNA accessibility than that of interacting genes, $P < 0.0001$; Fig. 2d,f) and displayed 56-fold lower expression levels than interacting genes ($P < 0.0001$; Fig. 2e). On the other hand, 47.6% of skipped genes in the forebrain were demethylated and accessible at their promoters, similar to promoters of interacting genes (Fig. 2d,f). These genes displayed expression levels comparable to those of interacting genes (Fig. 2e). We observed the same trends in all seven tissues for which matched expression and epigenomic data were available (Fig. 2d–f and Extended Data Fig. 4).

Interestingly, promoters of skipped genes did not display significantly higher levels of trimethylation at histone H3 lysine 27 (H3K27me3) or lysine 9 (H3K9me3) (Extended Data Fig. 4d,e), indicating that polycomb silencing and heterochromatin may not play a major role in regulating E–P selectivity. In sum, our data indicate that most developmental enhancers in our study bypass neighboring genes, which are often inactive and marked by promoter CpG methylation.
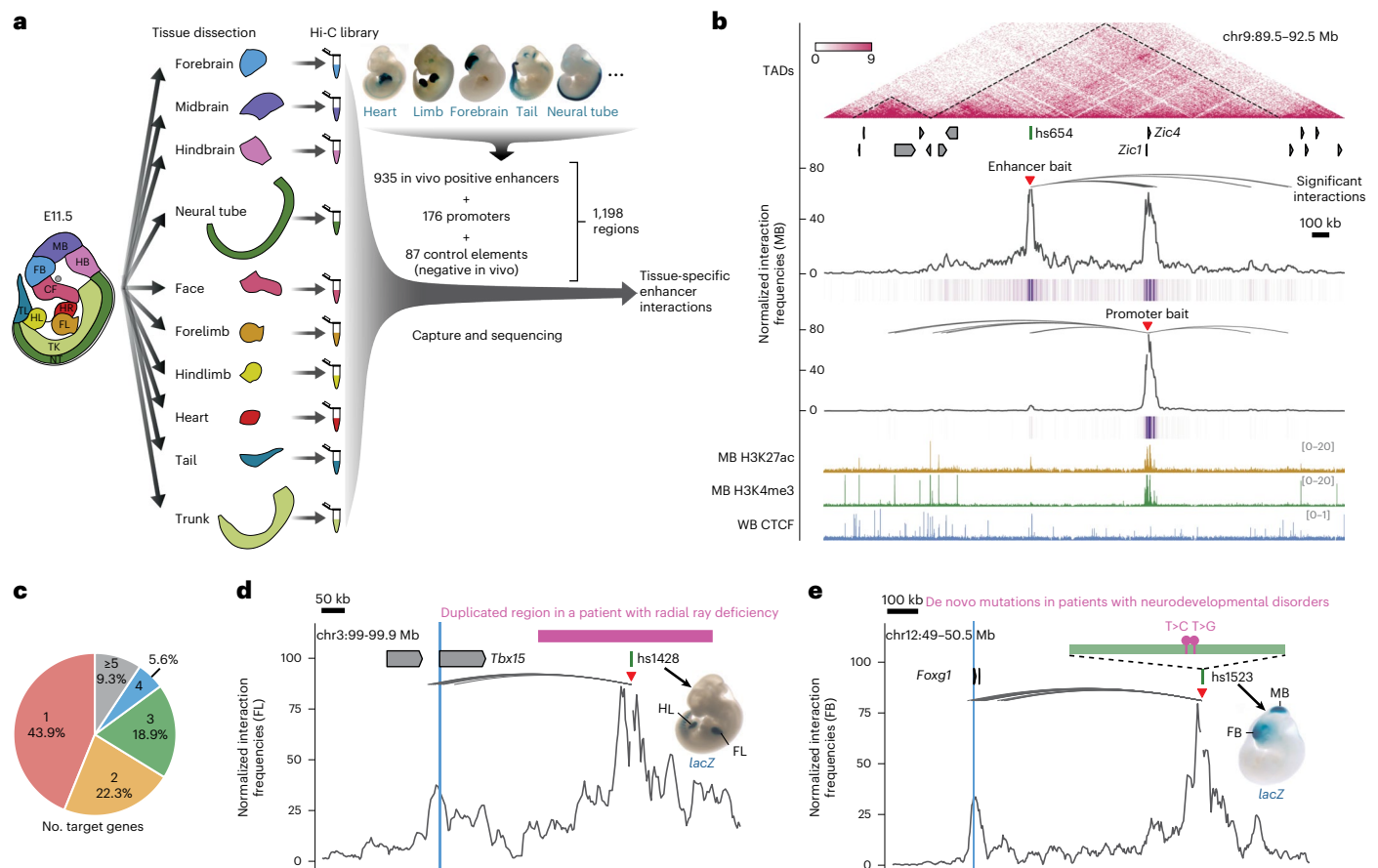
Fig. 1 | Identification of enhancer-centric chromatin interactions in ten mouse embryonic tissues. a, Experimental design. Ten tissue samples from mouse embryos at E11.5 were used to prepare Hi-C libraries followed by oligonucleotide capture with probes targeting 1,198 baited regions, including 935 enhancers (representative enhancer activities are shown above), 176 promoters and 87 control elements. CF, face; FB, forebrain; FL, forelimb; HB, hindbrain; HL, hindlimb; HR, heart; MB, midbrain; NT, neural tube; TK, trunk; TL, tail. **b**, Enhancer capture Hi-C identifies chromatin interactions of enhancers. A 3-Mb region containing the hs654 midbrain enhancer (chromosome (chr)9:89,500,000–92,500,000, mm10) is shown with the following annotations from top to bottom: TADs (dashed lines outline TAD boundaries)[72,73], RefSeq genes, normalized hs654-centered chromatin interaction frequencies in the midbrain shown as a plot and purple heatmap below, normalized *Zic1* and *Zic4* promoter-centered chromatin interaction frequencies, H3K27ac and histone 3 lysine 4 trimethylation (H3K4me3) chromatin immunoprecipitation followed by

sequencing (ChIP–seq) profiles in the midbrain at E11.5, CTCF ChIP–seq profile in whole brain (WB) at E12.5 (refs. 33,74,75). The average bin size is ~3 kb. Curved lines indicate significant interactions. **c**, Pie chart showing the percentage of enhancers interacting with different numbers of genes. **d**, The hs1428 limb enhancer (green box) is in a noncoding region that is duplicated in patients with radial ray deficiency (pink bar indicates the homologous region in the mouse genome). The hs1428 limb enhancer forms significant chromatin interactions with the promoter of *Tbx15* (highlighted in blue) located ~400 kb away (chr3:99,000,000–99,900,000, mm10)[76] in the forelimb. **e**, Two de novo rare variants identified in patients with neurodevelopmental disorders[77,78] are in the hs1523 forebrain–midbrain enhancer (green bar), which forms strong significant interactions with the promoter of *Foxg1* (highlighted in blue) located ~700 kb away (chr12:49,121,092–50,469,462, mm10) in the forebrain. Red arrowheads indicate capture Hi-C viewpoints.

Enhancer knockouts validate E–P chromatin interactions

To assess the functionality and specificity of identified E–P chromatin interactions, we created knockout mice for hs654, hs267, hs266 and hs853 brain enhancers (Fig. 3 and Extended Data Fig. 5). All four enhancers form significant chromatin interactions with promoters of their putative target genes in the mouse embryonic brain at E11.5 (*Zic1* and *Zic4* for hs654 and *Mir9-2* for hs267, hs266 and hs853; Figs. 1b and 4b and Extended Data Fig. 3a). We created two mouse knockout lines, one carrying a deletion of hs654 (Δhs654) and the other carrying a deletion of the hs267, hs266 and hs853 enhancers (Δhs267/hs266/hs853), and assessed tissue-specific gene expression by RNA-seq (Extended Data Fig. 5). In Δhs654/Δhs654 mice, *Zic4* RNA expression in the midbrain was reduced by ~34% compared with wild-type levels (adjusted P (P_{adj}) < 9.5 × 10^{-3}; Fig. 3c), supporting the functional relevance of the hs654–*Zic4* chromatin interaction in the embryonic midbrain. *Zic1* expression was reduced by ~18%, albeit not statistically significant, and no other genes were significantly downregulated or

upregulated in Δhs654/Δhs654 mice (Fig. 3c). Mice homozygous for the hs267/hs266/hs853 deletion showed downregulation of *C130071C03Rik* (*Mir-2* precursor transcript) by ~64% compared with the wild type (P_{adj} < 7.8 × 10^{-32}; Fig. 3d). Notably, there was no significant change in *Tmem161b* expression or any other gene in *cis*, indicating that these three enhancers specifically control the expression of *Mir9-2* as predicted by chromatin interactions between hs267/hs266/hs853 and the *Mir9-2* promoter but not the *Tmem161b* promoter (Extended Data Fig. 3a). Overall, the loss of enhancers results in a large decrease in transcription of interacting target genes, which supports the idea that E–P chromatin interactions identified by enhancer capture Hi-C are functional and specific.

Enhancer interactions are more frequent when enhancers are active in vivo

The general extent to which E–P interaction frequency correlates with in vivo enhancer activity at most developmental loci is unclear yet
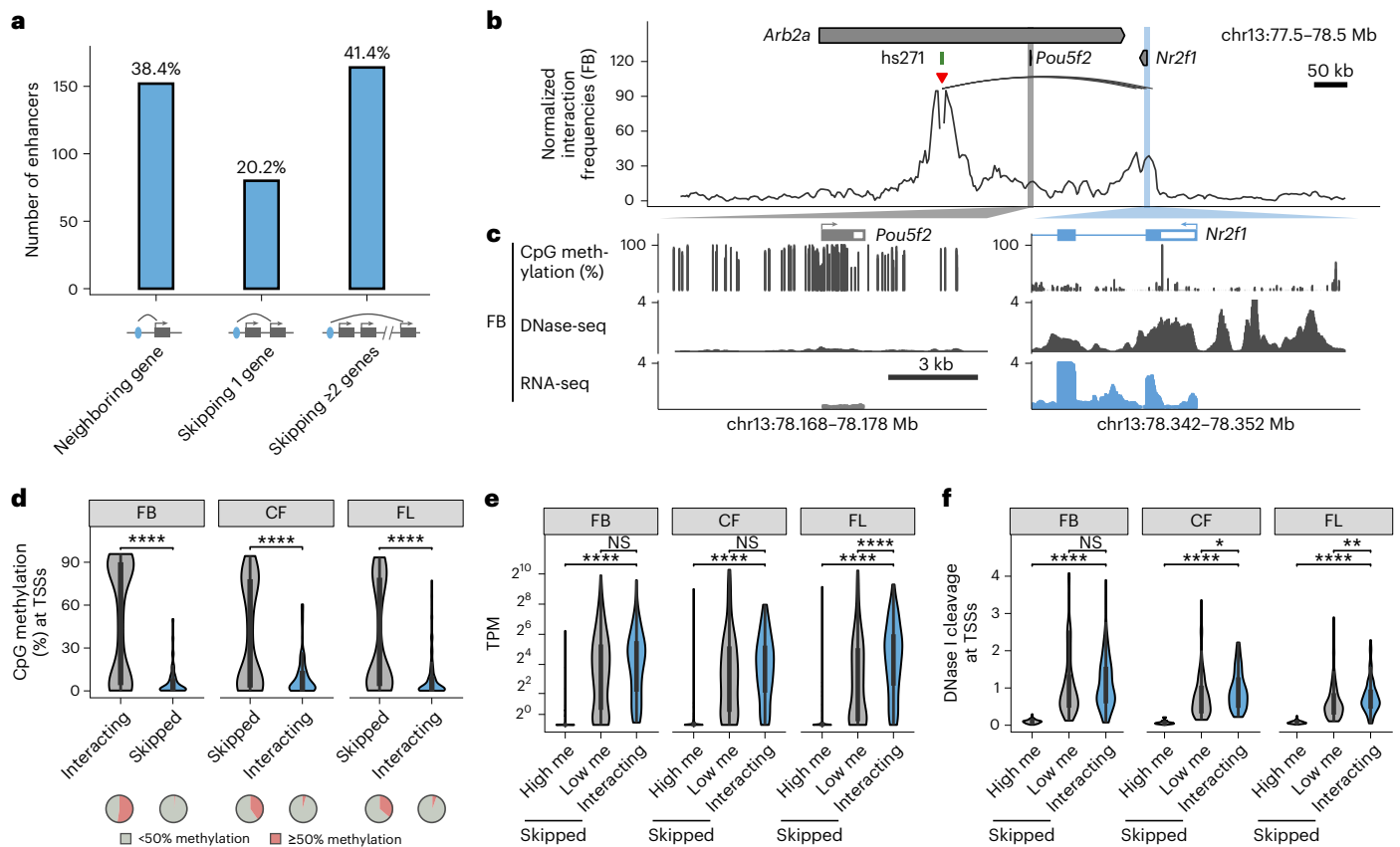
**Fig. 2 | Properties of promoters that are skipped by remote enhancers.**
a, Bar plot showing enhancers grouped by their genomic positions relative to the interacting genes. The diagram below shows corresponding schematic gene loci in which the enhancer (blue oval) interacts with a neighboring gene (left), skips one gene (middle) or skips two or more genes (right). Arches indicate significant interactions. **b**, Normalized capture Hi-C data from the viewpoint of the hs271 enhancer (red arrowhead) are shown with significant interactions (black arches) in the forebrain at E11.5 (chr13:77,500,000–78,500,000, mm10). *Pou5f2* and *Nr2f1* promoters are highlighted in gray and blue. **c**, CpG methylation, DNase-seq and RNA-seq profiles at *Pou5f2* and *Nr2f1* promoters in the forebrain at E11.5 (refs. 33,74,79). **d**–**f**, CpG methylation (**d**), mRNA expression levels (**e**, transcripts per million (TPM)) and DNase signal (**f**) of enhancer-interacting and skipped promoters in tissues where enhancers are active. The numbers of skipped and interacting promoters in **d** are $n = 265$ and $n = 90$ (FB, forebrain), $n = 144$ and $n = 71$

(CF, face) and $n = 182$ and $n = 96$ (FL, forelimb), and the P values are 3.6×10^{-17}, 3.9×10^{-7} and 2.2×10^{-11}, respectively. The numbers of high- and low-methylated skipped as well as interacting promoters in **e** are $n = 134$, $n = 121$ and $n = 90$ (FB), $n = 56$, $n = 81$ and $n = 71$ (CF) and $n = 64$, $n = 111$ and $n = 96$ (FL), and the P values are 1×10^{-35}, 1.3×10^{-18}, 6.9×10^{-22} and 6.4×10^{-5}, respectively. The numbers of high- and low-methylated skipped as well as interacting promoters in **f** are $n = 139$, $n = 126$ and $n = 90$ (FB), $n = 58$, $n = 86$ and $n = 71$ (CF) and $n = 66$, $n = 116$ and $n = 96$ (FL), and the P values are 2.4×10^{-34}, 2.9×10^{-22} and 0.012, 7.8×10^{-25} and 0.0039, respectively. High me or low me, high or low methylation at skipped promoters ($\geq 50\%$ or $<50\%$ CpG methylation within ± 1 kb from the TSS). NS, not significant. P values were calculated using the two-sided Wilcoxon rank test and adjusted for multiple testing. For box plots in **d**–**f**, the central horizontal lines are the median, with boxes extending from the 25th to the 75th percentiles. The whiskers further extend by ± 1.5 times the interquartile range from the limits of each box.

critical for understanding the spatiotemporal control of long-range gene regulation during development. To address this, we systematically compared tissue-specific enhancer activities with corresponding E–P interactions in different parts of the embryo. We selected 969 interacting E–P pairs identified by enhancer capture Hi-C for which gene expression matched enhancer activity in at least one tissue (Supplementary Table 2 and the Methods). We then systematically examined E–P chromatin interaction profiles in each of the ten tissues and compared them with the experimentally determined in vivo activities of the corresponding enhancers in each of these tissues. Clustering of 969 E–P interactions across ten tissues revealed a strong correlation with in vivo enhancer activities (logistic regression, $P = 9.7 \times 10^{-46}$; Fig. 4a and Extended Data Fig. 6b). Enhancers active in the central nervous system displayed higher interaction frequencies in the forebrain, midbrain, hindbrain and neural tube but not in other tissues (from 1.3-fold in the neural tube ($P = 7.3 \times 10^{-11}$) to 1.6-fold in the forebrain ($P = 1.03 \times 10^{-42}$); Fig. 4a,c,d and Extended Data Fig. 6a,h,f). For example, the hs654 enhancer predominantly contacted *Zic1* and *Zic4* genes in the brain, neural tube and tail, tissues where enhancer and gene were both active (Figs. 3a and 4b). Interaction between hs654 and

Zic1 or *Zic4* was largely absent in face, limbs and heart tissues where hs654, *Zic1* and *Zic4* are inactive (Fig. 4b)[34]. Similarly, limb-specific enhancers displayed higher interaction frequencies with promoters in limb tissue (1.62-fold, $P < 1.5 \times 10^{-37}$), heart-specific enhancers in the heart (1.3-fold, $P = 4.3 \times 10^{-9}$) and face-specific enhancers in the face (1.62-fold, $P = 3.6 \times 10^{-27}$) (Fig. 4a,d and Extended Data Fig. 6a). We observed this pattern (that enhancers form significantly more frequent interactions with their respective target promoters when enhancers are active) for most enhancers in eight of ten examined tissues (Fig. 4d and Extended Data Fig. 6a). There was no significant difference in interaction frequency for enhancers active in the tail and trunk, likely due to the low number of enhancers with characterized activity in these tissues (Extended Data Fig. 6a). We observed no significant increase in enhancer interactions with negative control regions in tissues where enhancers were active, confirming the specificity of these observed E–P interactions (Extended Data Fig. 6e).

We observed a similar trend even within developmentally related tissues, such as different parts of the brain. Enhancers active only in specific areas of the developing brain formed significantly more frequent interactions with promoters in those tissues than with those in
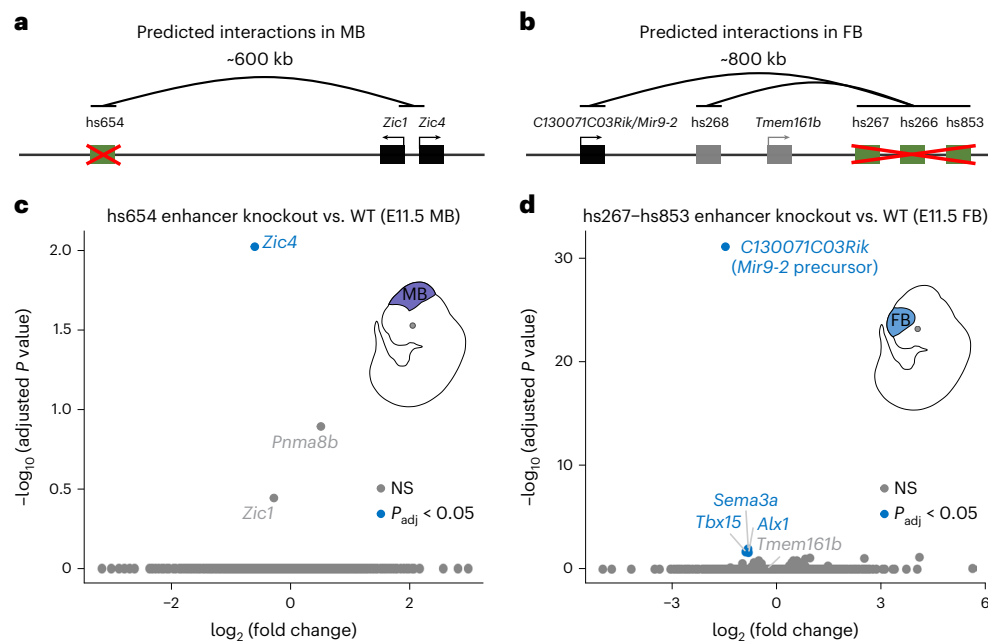
Fig. 3 | Enhancers are required for expression of interacting genes. Knockout analysis of hs654 and hs267/hs266/hs853 enhancers. **a,b**, Predicted chromatin interactions (black arches) between hs654 (**a**) and hs267/hs266/hs853 (**b**) enhancers (green boxes) and target genes (black boxes) are shown. Gene and enhancer models are not drawn to scale. **c,d**, Transcriptome-wide mRNA expression changes at E11.5 in the whole midbrain of hs654-knockout mice (**c**) and at E11.5 in the forebrain of hs267/hs266/hs853-knockout mice (**d**) relative to wild-type mice (WT). Points indicate individual genes, with blue indicating statistically significant differences after adjustment for multiple comparisons ($P_{adj} < 0.05$). P values were calculated using DESeq2.

parts of the brain where those enhancers were inactive (1.68-fold in the forebrain ($P = 3.5 \times 10^{-8}$) and 1.19-fold in the hindbrain ($P = 0.027$)), with the exception of the midbrain (Extended Data Fig. 6i,j). Notably, a small fraction of enhancers that formed invariant interactions with promoters across all tissues displayed an increased frequency of these interactions in tissues where the enhancer was active in vivo (Extended Data Fig. 7a,b). These results indicate that developmental gene activation is generally associated with increased interaction frequency between corresponding enhancers and their target promoters.

We next examined in vivo chromatin interactions between enhancers (E–E contacts), including enhancers predicted based on chromatin features such as acetylation of histone 3 lysine 27 (H3K27ac). Previous studies suggest a model in which enhancers regulating the same gene in the same cell form multi-enhancer hubs to activate gene expression[16,35,36]. We observed that E–E contacts formed between enhancers with overlapping activities are likely to regulate the same gene (Extended Data Fig. 3). For example, the hs268, hs267, hs266 and hs853 enhancers, which are located in the same TAD, formed extensive significant interactions with the promoter of the *Mir9-2* gene (Extended Data Fig. 3a). All four enhancers were active in the dorsal telencephalon, and their activity patterns were strikingly similar to the expression of the *Mir9-2* precursor (Extended Data Fig. 3a,c). All four enhancers also formed extensive interactions with each other in the forebrain (Extended Data Fig. 3a), but these E–E interactions were virtually absent in developing limb buds where *Mir9-2* is not expressed, suggesting that these four enhancers form a multi-enhancer hub (Extended Data Fig. 3b). We observed similar tissue-specific E–E interactions in other loci and tissues (Extended Data Fig. 3d,e). Generally, enhancers formed significantly stronger interactions with other enhancers when they were active in the brain, face or limb (Fig. 4e,f and Extended Data Fig. 8b). These results are consistent with a model in which increased interactions among multiple enhancers during mammalian development and a given promoter accompanies transcriptional activation.

Decrease in E–P distance in tissues where enhancers are active

To test whether the increased E–P interactions also results in a change in physical distance between enhancers and promoters[37,38], we used super-resolution microscopy in conjunction with fluorescence in situ hybridization (FISH) on 3D preserved nuclei (3D-FISH) to visualize enhancers and promoters in developing mouse embryos. We chose three independent genetic loci where enhancer capture Hi-C revealed tissue-specific interactions between enhancers and their target genes (*Zic1* and *Zic4*, Fig. 4b; *Mir9-2*, Extended Data Fig. 3a; *Snai2*, Fig. 6a). For all three genetic loci, the regulatory connection between enhancers and the corresponding target genes was independently confirmed using enhancer-knockout experiments (Fig. 3)[28].

We performed 3D-FISH in forebrain, midbrain, face and forelimb cells at E11.5 using fosmid-based probes targeting hs654, hs266 and hs1431 enhancers and the corresponding target promoters. We observed a significant decrease in interprobe distance ($P = 1.18 \times 10^{-4}$, hs654–*Zic1/Zic4* pair; $P = 9.53 \times 10^{-7}$, hs266–*Mir9-2* pair; $P = 0.0106$, hs1431–*Snai2* pair) and an increase in the fraction of colocalized alleles in tissues where the corresponding enhancers were active for all three genetic loci (Fig. 5a,b and Extended Data Fig. 6n–p). For example, for the hs266–*Mir9-2* pair, the fraction of alleles with interprobe distances less than 250 nm was 20% in the forelimb and increased to 32% in the forebrain ($P = 1.47 \times 10^{-3}$) where *Mir9-2* is active (Fig. 5b and Extended Data Fig. 6o). A similar trend was observed for the hs654–*Zic1/Zic4* pair (28% in the midbrain versus 20% in the forelimb; $P = 0.0132$) and for the hs1431–*Snai2* pair (32% in the face versus 24% in the forebrain; not significant) (Fig. 5b and Extended Data Fig. 6n,p). In sum, our 3D-FISH experiments showed a significant decrease in E–P physical distance in tissues where enhancers were active, which supports the increase in E–P interactions observed in our proximity ligation-based enhancer capture Hi-C experiments.

Properties of invariant E–P interactions

Widespread stable mammalian E–P loops have been reported for enhancers and predicted from chromatin features in mouse
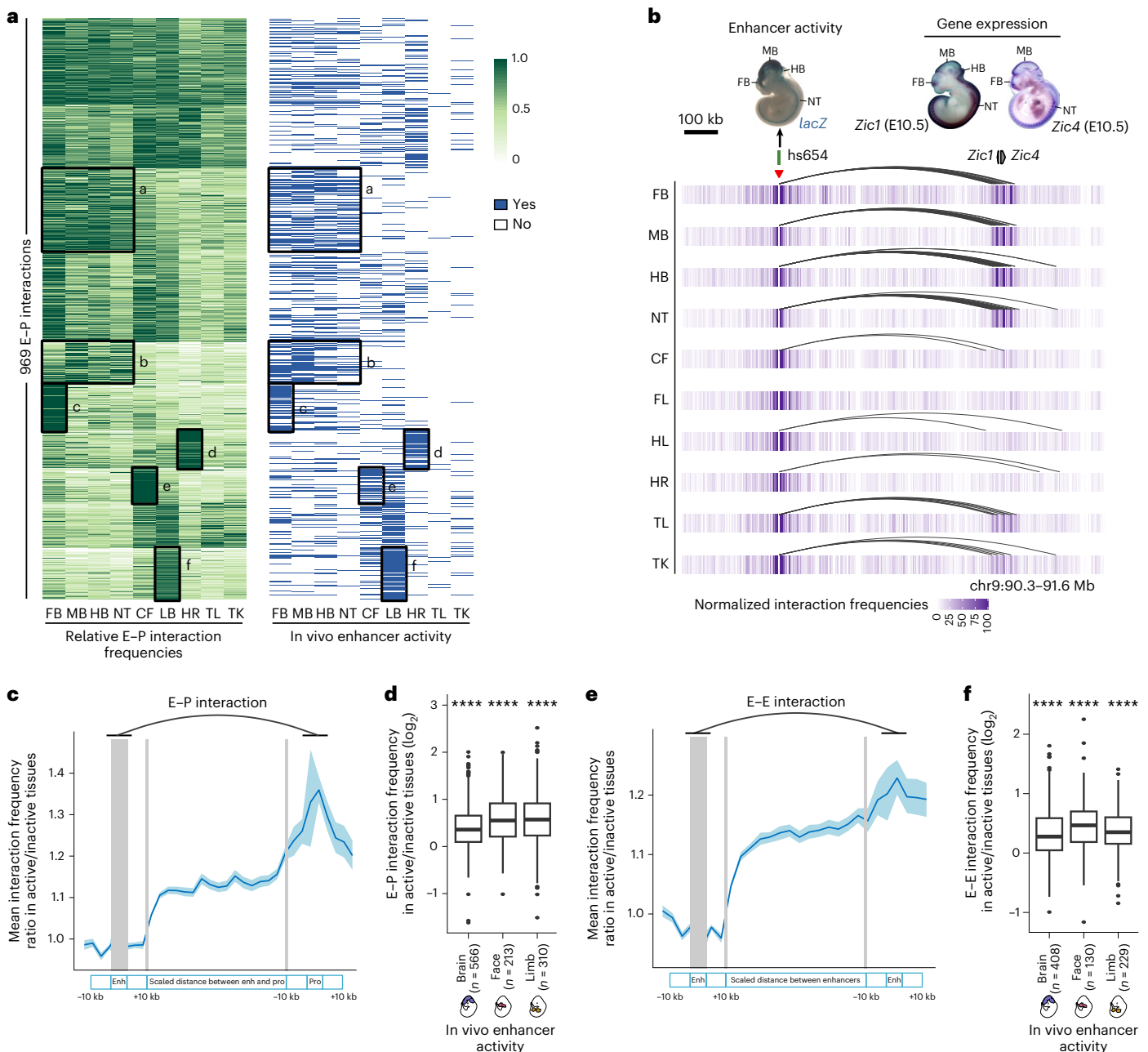
Fig. 4 | Tissue specificity of developmental enhancer interactions. a, Heatmap showing relative E–P chromatin interaction frequencies (scaled to the maximum value among tissues in each E–P interaction, green) and in vivo enhancer activities (blue) of 969 E–P chromatin interactions. *k*-means clustering (*k* = 10) was performed on interaction frequencies. The six highlighted tissue-specific interaction clusters match in vivo enhancer activities. LB, limb bud. **b**, Interaction profiles across ten tissues centered on the hs654 enhancer (red arrowhead indicates the capture Hi-C viewpoint). Top left, hs654 enhancer activity in a transgenic mid-gestation (E11.5) mouse embryo. Top right, *Zic1* and *Zic4* mRNA whole-mount in situ hybridization (WISH) at E10.5 (images reproduced with permission from the Gene Expression Database (*Zic4*)[34] and the EMBRYS database (http://embrys.jp; *Zic1*). Heatmaps with normalized interaction frequencies in each of the ten tissues are shown below. Curved lines indicate

significant interactions. **c**,**e**, Average ratio of E–P (**c**) or E–E (**e**) interaction frequency between active and inactive tissues based on the analysis of 946 E–P or 640 E–E chromatin interactions is shown (see the Methods for details of the normalization procedure). Light blue shading indicates 95% confidence intervals estimated by nonparametric bootstrapping. Enh, enhancer; pro, promoter. **d**,**f**, Average ratio of E–P (**d**) or E–E (**f**) interaction frequency between active and inactive tissues for enhancers active in brain, face and limb (see Extended Data Figs. 6a and 8b for other tissues). *P* values for E–P interactions are 5.07×10^{-61} (brain), 6.1×10^{-28} (face) and 6.21×10^{-43} (limb). *P* values for E–E interactions are 3.3×10^{-38} (brain), 1×10^{-17} (face) and 1.5×10^{-29} (limb). For the box plots in **d**,**f**, central horizontal lines are the median, with boxes extending from the 25th to the 75th percentiles. The whiskers further extend by ±1.5 times the interquartile range from the limits of each box.

embryonic limbs and brain[20], mouse embryonic stem cells[39,40] and human keratinocytes[17]. However, how common stable E–P looping is at most developmental loci is unknown. Our analysis of E–P chromatin interactions for bona fide developmental enhancers found that only a small fraction (13.3%) formed tissue-invariant loops across all ten examined embryonic tissues (Fig. 6a–d). Nevertheless,

these invariant E–P interactions displayed higher interaction frequency in tissues where enhancers were active (Extended Data Fig. 7a,b).

Stable E–P chromatin interactions are often associated with neighboring CTCF binding[20,39–41]. Indeed, we observed that tissue-invariant interactions in E11.5 mouse embryos are also associated with
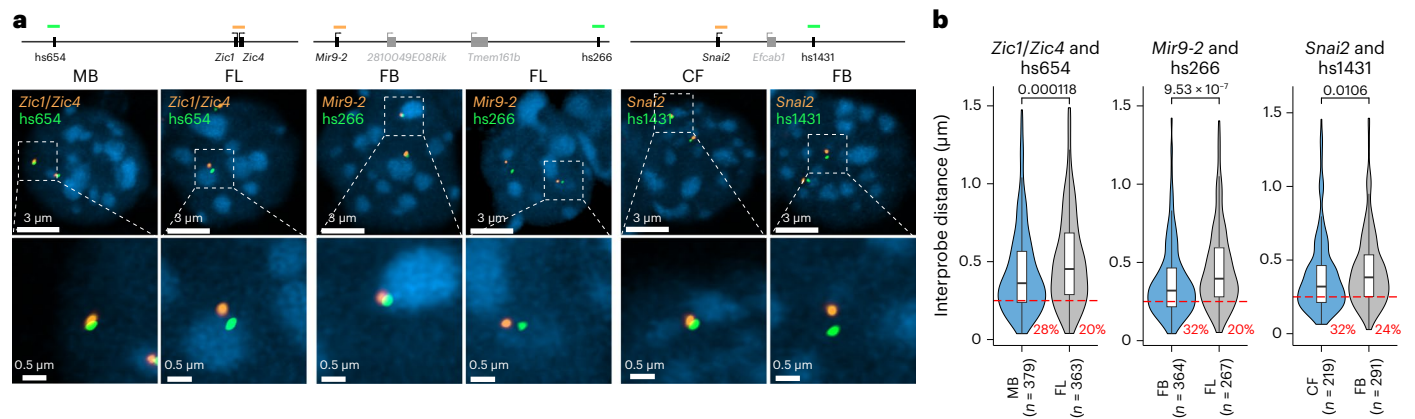
Fig. 5 | Imaging E–P interactions in the developing mouse embryo.
a, Genomic positions of probes labeling enhancers (green) and genes (orange) are shown on the top. Gene and enhancer models are not drawn to scale. Images of representative nuclei (4,6-diamidino-2-phenylindole (DAPI), blue) at E11.5 from the midbrain (left) and forelimb (right) after FISH with *Zic1*, *Zic4* and hs654 probe pairs (left), at E11.5 from the forebrain (left) and forelimb (right) after FISH with *Mir9-2* and hs266 probe pairs (middle) and at E11.5 from the face (left) and forebrain (right) after FISH with *Snai2* and hs1431 probe pairs (right) are shown. Corresponding magnified images are shown below. **b**, Violin plot showing the distribution of interprobe distance (µm) between fosmid probe pairs in active

and inactive tissues. Red dashed lines indicate colocalization (<0.25 µm), and the numbers below represent the fraction of loci with colocalized probes. *P* values were calculated with paired-sample two-sided Wilcoxon test and adjusted for multiple testing for comparison of interaction frequencies between active and inactive tissues; unpaired-sample two-sided Wilcoxon test was performed for comparison of interprobe distance between different tissues. For box plots in **b**, central horizontal lines are the median, with boxes extending from the 25th to the 75th percentiles. The whiskers further extend by ±1.5 times the interquartile range from the limits of each box.

proximal CTCF binding, with more than 85% of all invariant interactions having proximal (<5 kb) CTCF binding at either end (Fig. 6b–e). By comparison, less than 50% of tissue-specific interactions overlapped CTCF (Fig. 6e). The vast majority (87 of 98, 88.8%) of enhancers that formed invariant interactions were active only in a subset of tissues, similar to enhancers that form tissue-specific contacts (Extended Data Fig. 7c), which is consistent with a model in which CTCF forms these invariant interactions independently of enhancer activity.

To test whether tissue-invariant interactions form independently of enhancer activity, we experimentally assessed how these E–P chromatin contacts are affected by targeted deletion of the enhancer. We chose the *Shh* locus, where a limb-specific ZRS enhancer forms chromatin interactions with the *Shh* promoter located ~850 kb away in all ten examined tissues (Fig. 6c). We generated a knockin mouse line in which the entire ZRS enhancer was replaced with a piece of non-mouse DNA lacking any regulatory activity to simultaneously eliminate the enhancer and enable allele-specific detection of chromatin interactions in capture Hi-C experiments. For that purpose, we used part of the bacterial *lacZ* gene sequence. Mice homozygous for the ZRS*lacZ* allele showed no detectable *Shh* expression in limb buds and displayed reduced limb buds at E11.5 and truncated zeugopods and autopods at E18.5, which is consistent with complete loss of *Shh* in the limb (Fig. 6f and Extended Data Fig. 9)[42]. To determine whether ZRS enhancer activity contributes to its higher-order chromatin interactions with the *Shh* promoter, we performed capture Hi-C experiments in fully developed limb buds of mice heterozygous for the ZRS*lacZ* allele at E11.5. Using probes targeting both the wild-type ZRS and the *lacZ* sequence, we found that both the wild-type ZRS allele and the 'enhancerless' *lacZ* allele formed significant interactions with the *Shh* promoter (Fig. 6h). These results demonstrate that the higher-order chromatin interaction between ZRS and *Shh* can form independently of ZRS enhancer activity.

Discussion

In this study, we comprehensively determined tissue-resolved in vivo interaction landscapes for 935 bona fide enhancers, thus identifying thousands of tissue-specific interactions. Enhancer 3D chromatin

conformations are highly dynamic across tissues and mirror the highly tissue-specific activity patterns observed for these enhancers in transgenic mouse embryos. We find moderate but consistent increases in E–P and E–E interactions in tissues where enhancers are functionally active. Together, our chromatin interaction data for 935 enhancers suggest that E–P physical proximity is a general feature of developmental gene activation in mammals.

Notably, we also detected E–P chromatin interactions that are tissue invariant and are associated with proximal CTCF binding. Similar stable loops have been reported for other mammalian loci[17,20,21,41], where they likely provide an additional level of robustness to maintain stable levels of gene expression during development[41]. Our data on bona fide enhancers suggest that these interactions occur next to a smaller fraction of developmental enhancers and likely form independently of enhancer activity. As both tissue-invariant CTCF–cohesin-bound loops formed by loop extrusion and enhancer loops are widespread in the genome[43], it is plausible that many of them overlap. Indeed, we did not observe differences in tissue specificity, evolutionary DNA conservation or classes of target genes between enhancers that form tissue-invariant chromatin contacts and enhancers that form tissue-specific chromatin interactions with their promoters (Extended Data Fig. 7c–e).

While an increase in E–P interactions is linked to gene activation, the average observed increase in E–P contact frequency between active and inactive tissues appears to be less than 1.5-fold (Fig. 4c), even though average changes in associated tissue-specific gene expression are ~11-fold (Extended Data Fig. 6g). Several models have been proposed to explain this nonlinear relationship between E–P contact probability and transcription, including bistability, hysteresis and transient two-state E–P interactions[44,45]. The association between direct E–P contact and transcription at the macromolecular level remains elusive, as some genetic loci show no association or reverse association between E–P physical distance and transcription[23–25]. At least some differences could be due to the different approaches used to measure E–P interactions. Hi-C-based methods are based on proximity ligation and can be biased by cross-linking efficiency, while imaging-based methods, such as FISH, measure E–P distance directly. The two approaches sometimes result in contradicting results[25,37,38,46]. Higher-resolution imaging techniques and chromatin conformation capture methods as
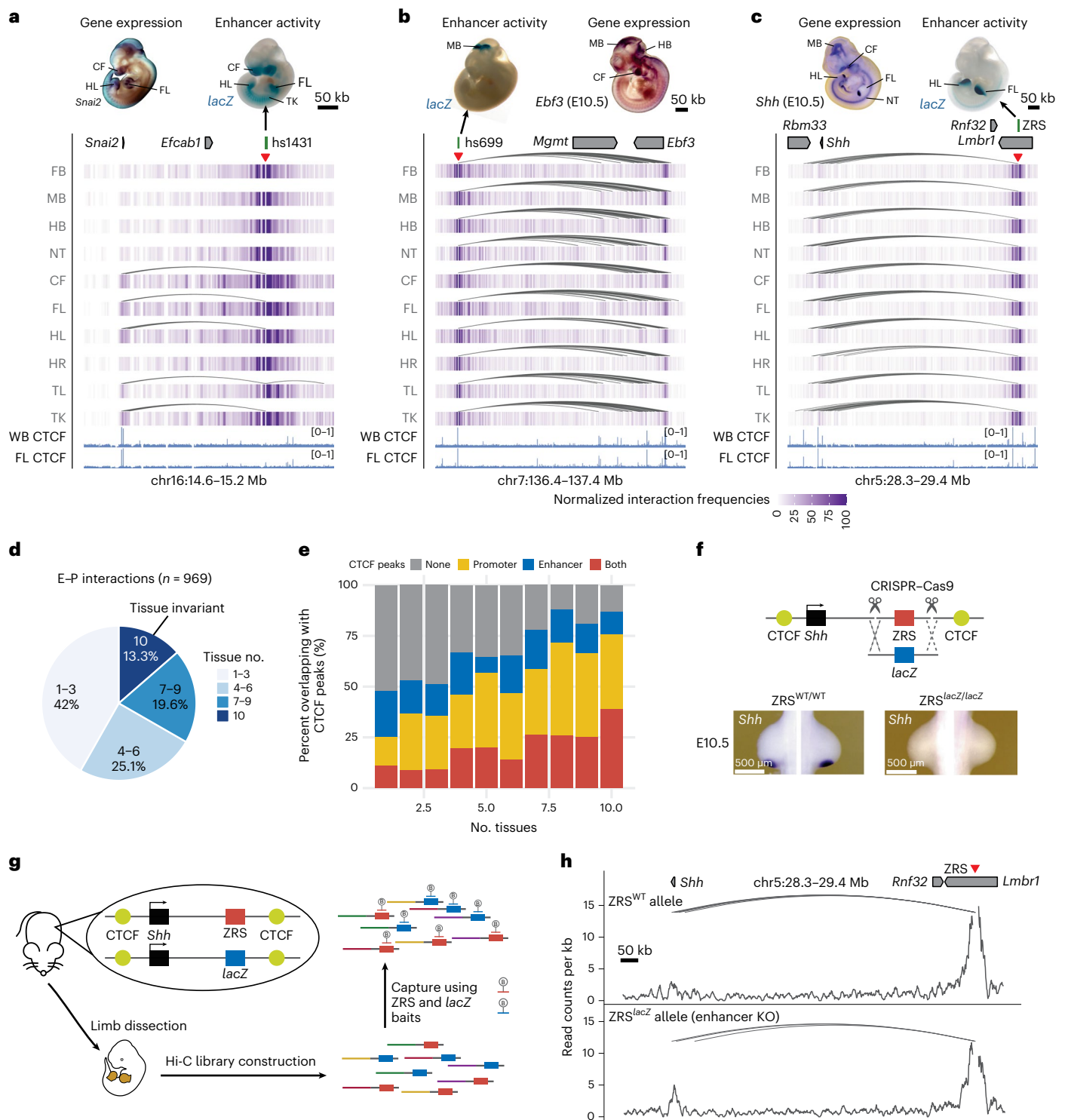
Fig. 6 | Properties of tissue-invariant E–P chromatin interactions.
a–c, Chromatin interaction profiles across ten tissues centered on the hs1431 enhancer in the *Snai2* locus (chr16:14,610,000–15,220,000, mm10) (**a**), the hs699 enhancer in the *Dlx5* and *Dlx6* locus (chr7:136,400,000–137,400,000, mm10) (**b**) and the ZRS enhancer in the *Shh* locus (chr5:28,320,000–29,400,000, mm10) (**c**). Shown above are corresponding enhancer activities in transgenic mouse embryos at E11.5 and the corresponding interacting gene mRNA WISH in embryos at E11.5 or E10.5. Heatmaps with normalized interaction frequencies in each of the ten tissues are shown below. CTCF ChIP–seq profiles (blue) in the whole brain and forelimb at E12.5 are shown at the bottom[75]. Arches indicate significant interactions. Red arrowheads depict capture Hi-C viewpoints. **d**, Pie chart showing the fraction of E–P interactions present in different numbers of tissues. **e**, Fraction of E–P interactions that overlap with CTCF peaks grouped by number of tissues in which

the interaction was detected. **f**, Schematic of the Cas9-mediated strategy for replacement of the mouse ZRS sequence (red box) with a fragment of the bacterial *lacZ* gene (blue box) at the *Shh* (black) genomic locus. CTCF-binding sites are indicated in yellow. *Shh* mRNA WISH analysis in wild-type and ZRS^*lacZ/lacZ* mouse forelimb buds at E10.5 are shown below. See Extended Data Fig. 9 for details. **g**, Schematic overview of the capture Hi-C approach to detect chromatin interactions in the presence and absence of the ZRS in limbs of the same mouse using biotinylated RNA probes (B) targeting ZRS and *lacZ*. Limb buds from heterozygous transgenic mice were dissected followed by capture Hi-C to enrich for ZRS and *lacZ* interactions. **h**, Allele-specific ZRS region-centric chromatin interactions in limb buds of ZRS^*+/lacZ* mice at E11.5. Arches indicate significant interactions. WISH images in **a,b** have been reproduced with permission from the Gene Expression Database (*Ebf3*)[34] and the EMBRYS database (http://embrys.jp; *Snai2*). KO, knockout.

well as methods based on live imaging will be needed to untangle complex relationships between direct E–P contacts and transcription[47–50].

Our results contrast with other systems such as early *Drosophila* embryo development[19,51,52] or stimulus-induced gene activation[53,54], where E–P loops appear to be stable and are often associated with paused polymerase II[19]. In these specialized systems, preformed E–P topologies might ensure robust and rapid gene activation[12,19]. Interestingly, the emergence of new E–P loops correlates with enhancer activation in differentiated *Drosophila* embryonic tissues, suggesting that E–P proximity could be an evolutionary conserved property of mid–late animal embryogenesis[55].

More than half of the developmental enhancers in our study appear to skip neighboring genes to regulate a more distal one. Such interactions have also been reported in mice[56,57] and humans[58,59] and to a lesser degree in *Drosophila*[60,61]. This raises the question: how is this E–P selectivity achieved? Our analysis of remote E–P interactions shows that promoters of approximately half of the skipped genes are methylated and inaccessible (Fig. 2d–f and Extended Data Fig. 4), suggesting that promoter silencing could potentially be one of the mechanisms by which such enhancer–gene specificity is achieved in mammals[62]. However, the other half of promoters skipped by distal enhancers are not methylated and are accessible at levels comparable with those of target genes, indicating that additional factors facilitate promoter bypassing by remote enhancers. Such factors could potentially include compatibility between enhancers and different types of core promoters[63–66] and tethering elements[61,67,68]. The general mechanism that determines E–P specificity in mammalian genomes is still poorly understood[69], and further studies are needed to dissect how divergent expression is achieved within the same TAD. Notably, we also observe that 21% of developmental enhancers act across TAD boundaries, confirming previous observations[70,71]. These cross-TAD enhancers behave similarly to intra-TAD enhancers (Extended Data Fig. 6c) but tend to be located closer to TAD borders (Extended Data Fig. 6d), consistent with the boundary-staking model that was proposed to facilitate TAD border bypass[71].

It is important to note that the current study surveyed a relatively small fraction of bona fide developmental enhancers in a limited number of mouse embryonic tissues and time points. In future studies, functional characterization of a greater number of developmental enhancers and their chromatin interactions in vivo in various tissue and cell contexts will greatly aid functional interpretation of germline variants associated with human congenital disorders. Nonetheless, the current study provides a broad snapshot of the general 3D chromatin organization and properties of enhancers at typical developmental loci.

Online content

Any methods, additional references, Nature Portfolio reporting summaries, source data, extended data, supplementary information, acknowledgements, peer review information; details of author contributions and competing interests; and statements of data and code availability are available at https://doi.org/10.1038/s41588-024-01681-2.

References

1. Lettice, L. A. et al. Disruption of a long-range *cis*-acting regulator for *Shh* causes preaxial polydactyly. *Proc. Natl Acad. Sci. USA* **99**, 7548–7553 (2002).
2. Long, H. K. et al. Loss of extreme long-range enhancers in human neural crest drives a craniofacial disorder. *Cell Stem Cell* **27**, 765–783 (2020).
3. Shlyueva, D., Stampfel, G. & Stark, A. Transcriptional enhancers: from properties to genome-wide predictions. *Nat. Rev. Genet.* **15**, 272–286 (2014).
4. Long, H. K., Prescott, S. L. & Wysocka, J. Ever-changing landscapes: transcriptional enhancers in development and evolution. *Cell* **167**, 1170–1187 (2016).
5. Schoenfelder, S. & Fraser, P. Long-range enhancer–promoter contacts in gene expression control. *Nat. Rev. Genet.* **20**, 437–455 (2019).
6. Dixon, J. R. et al. Topological domains in mammalian genomes identified by analysis of chromatin interactions. *Nature* **485**, 376–380 (2012).
7. Nora, E. P. et al. Spatial partitioning of the regulatory landscape of the X-inactivation centre. *Nature* **485**, 381–385 (2012).
8. Lupiáñez, D. G. et al. Disruptions of topological chromatin domains cause pathogenic rewiring of gene–enhancer interactions. *Cell* **161**, 1012–1025 (2015).
9. Lettice, L. A. et al. Enhancer-adoption as a mechanism of human developmental disease. *Hum. Mutat.* **32**, 1492–1499 (2011).
10. Northcott, P. A. et al. Enhancer hijacking activates GFI1 family oncogenes in medulloblastoma. *Nature* **511**, 428–434 (2014).
11. Bulger, M. & Groudine, M. Looping versus linking: toward a model for long-distance gene activation. *Genes Dev.* **13**, 2465–2477 (1999).
12. Furlong, E. E. M. & Levine, M. Developmental enhancers and chromosome topology. *Science* **361**, 1341–1345 (2018).
13. Oudelaar, A. M. & Higgs, D. R. The relationship between genome structure and function. *Nat. Rev. Genet.* **22**, 154–168 (2021).
14. Andrey, G. et al. A switch between topological domains underlies *HoxD* genes collinearity in mouse limbs. *Science* **340**, 1234167 (2013).
15. Tolhuis, B., Palstra, R. J., Splinter, E., Grosveld, F. & de Laat, W. Looping and interaction between hypersensitive sites in the active β-globin locus. *Mol. Cell* **10**, 1453–1465 (2002).
16. Madsen, J. G. S. et al. Highly interconnected enhancer communities control lineage-determining genes in human mesenchymal stem cells. *Nat. Genet.* **52**, 1227–1238 (2020).
17. Rubin, A. J. et al. Lineage-specific dynamic and pre-established enhancer–promoter contacts cooperate in terminal differentiation. *Nat. Genet.* **49**, 1522–1528 (2017).
18. Deng, W. et al. Reactivation of developmentally silenced globin genes by forced chromatin looping. *Cell* **158**, 849–860 (2014).
19. Ghavi-Helm, Y. et al. Enhancer loops appear stable during development and are associated with paused polymerase. *Nature* **512**, 96–100 (2014).
20. Andrey, G. et al. Characterization of hundreds of regulatory landscapes in developing limbs reveals two regimes of chromatin folding. *Genome Res.* **27**, 223–233 (2017).
21. Jin, F. et al. A high-resolution map of the three-dimensional chromatin interactome in human cells. *Nature* **503**, 290–294 (2013).
22. Montavon, T. et al. A regulatory archipelago controls *Hox* genes transcription in digits. *Cell* **147**, 1132–1145 (2011).
23. Alexander, J. M. et al. Live-cell imaging reveals enhancer-dependent Sox2 transcription in the absence of enhancer proximity. *eLife* **8**, e41769 (2019).
24. Benabdallah, N. S. et al. Decreased enhancer–promoter proximity accompanying enhancer activation. *Mol. Cell* **76**, 473–484 (2019).
25. Gómez Acuña, L. I., Flyamer, I., Boyle, S., Friman, E. T. & Bickmore, W. A. Transcription decouples estrogen-dependent changes in enhancer–promoter contact frequencies and physical proximity. Preprint at *bioRxiv* https://doi.org/10.1101/2023.03.29.534720 (2023).
26. Zaugg, J. B. et al. Current challenges in understanding the role of enhancers in disease. *Nat. Struct. Mol. Biol.* **29**, 1148–1158 (2022).
27. Visel, A., Minovitsky, S., Dubchak, I. & Pennacchio, L. A. VISTA Enhancer Browser—a database of tissue-specific human enhancers. *Nucleic Acids Res.* **35**, D88–D92 (2006).
28. Attanasio, C. et al. Fine tuning of craniofacial morphology by distant-acting enhancers. *Science* **342**, 1241006 (2013).

29. Dickel, D. E. et al. Genome-wide compendium and functional assessment of in vivo heart enhancers. *Nat. Commun.* **7**, 12923 (2016).

30. Dickel, D. E. et al. Ultraconserved enhancers are required for normal development. *Cell* **172**, 491–499 (2018).

31. Kvon, E. Z. et al. Progressive loss of function in a limb enhancer during snake evolution. *Cell* **167**, 633–642 (2016).

32. Osterwalder, M. et al. Enhancer redundancy provides phenotypic robustness in mammalian development. *Nature* **554**, 239–243 (2018).

33. Gorkin, D. U. et al. An atlas of dynamic chromatin landscapes in mouse fetal development. *Nature* **583**, 744–751 (2020).

34. Smith, C. M. et al. The mouse Gene Expression Database (GXD): 2014 update. *Nucleic Acids Res.* **42**, D818–D824 (2014).

35. Kvon, E. Z., Waymack, R., Gad, M. & Wunderlich, Z. Enhancer redundancy in development and disease. *Nat. Rev. Genet.* **22**, 324–336 (2021).

36. Hnisz, D., Shrinivas, K., Young, R. A., Chakraborty, A. K. & Sharp, P. A. A phase separation model for transcriptional control. *Cell* **169**, 13–23 (2017).

37. Fudenberg, G. & Imakaev, M. FISH-ing for captured contacts: towards reconciling FISH and 3C. *Nat. Methods* **14**, 673–678 (2017).

38. Giorgetti, L. & Heard, E. Closing the loop: 3C versus DNA FISH. *Genome Biol.* **17**, 215 (2016).

39. Kubo, N. et al. Promoter-proximal CTCF binding promotes distal enhancer-dependent gene activation. *Nat. Struct. Mol. Biol.* **28**, 152–161 (2021).

40. Rao, S. S. P. et al. A 3D map of the human genome at kilobase resolution reveals principles of chromatin looping. *Cell* **159**, 1665–1680 (2014).

41. Paliou, C. et al. Preformed chromatin topology assists transcriptional robustness of *Shh* during limb development. *Proc. Natl Acad. Sci. USA* **116**, 12390–12399 (2019).

42. Sagai, T., Hosoya, M., Mizushina, Y., Tamura, M. & Shiroishi, T. Elimination of a long-range *cis*-regulatory module causes complete loss of limb-specific *Shh* expression and truncation of the mouse limb. *Development* **132**, 797–803 (2005).

43. Hsieh, T.-H. S. et al. Enhancer–promoter interactions and transcription are largely maintained upon acute loss of CTCF, cohesin, WAPL or YY1. *Nat. Genet.* **54**, 1919–1932 (2022).

44. Zuin, J. et al. Nonlinear control of transcription through enhancer–promoter interactions. *Nature* **604**, 571–577 (2022).

45. Xiao, J. Y., Hafner, A. & Boettiger, A. N. How subtle changes in 3D structure can create large changes in transcription. *eLife* **10**, e64320 (2021).

46. Williamson, I. et al. Spatial genome organization: contrasting views from chromosome conformation capture and fluorescence in situ hybridization. *Genes Dev.* **28**, 2778–2791 (2014).

47. Brandão, H. B., Gabriele, M. & Hansen, A. S. Tracking and interpreting long-range chromatin interactions with super-resolution live-cell imaging. *Curr. Opin. Cell Biol.* **70**, 18–26 (2021).

48. Chen, L.-F., Lee, J. & Boettiger, A. Recent progress and challenges in single-cell imaging of enhancer–promoter interaction. *Curr. Opin. Genet. Dev.* **79**, 102023 (2023).

49. Jerkovic, I. & Cavalli, G. Understanding 3D genome organization by multidisciplinary methods. *Nat. Rev. Mol. Cell Biol.* **22**, 511–528 (2021).

50. Pownall, M. E. et al. Chromatin expansion microscopy reveals nanoscale organization of transcription and chromatin. *Science* **381**, 92–100 (2023).

51. Espinola, S. M. et al. *Cis*-regulatory chromatin loops arise before TADs and gene activation, and are independent of cell fate during early *Drosophila* development. *Nat. Genet.* **53**, 477–486 (2021).

52. Simmons, E. et al. Independence of chromatin conformation and gene regulation during *Drosophila* dorsoventral patterning. *Nat. Genet.* **53**, 487–499 (2021).

53. Platt, J. L. et al. Capture-C reveals preformed chromatin interactions between HIF-binding sites and distant promoters. *EMBO Rep.* **17**, 1410–1421 (2016).

54. Ray, J. et al. Chromatin conformation remains stable upon extensive transcriptional changes driven by heat shock. *Proc. Natl Acad. Sci. USA* **116**, 19431–19439 (2019).

55. Pollex, T. et al. New enhancer–promoter interactions are gained during tissue differentiation and reflect changes in E/P activity. Preprint at *bioRxiv* https://doi.org/10.1101/2022.12.07.519443 (2022).

56. Smemo, S. et al. Obesity-associated variants within *FTO* form long-range functional connections with *IRX3*. *Nature* **507**, 371–375 (2014).

57. Birnbaum, R. Y. et al. Functional characterization of tissue-specific enhancers in the *DLX5/6* locus. *Hum. Mol. Genet.* **21**, 4930–4938 (2012).

58. Lettice, L. A. et al. A long-range *Shh* enhancer regulates expression in the developing limb and fin and is associated with preaxial polydactyly. *Hum. Mol. Genet.* **12**, 1725–1735 (2003).

59. Li, G. et al. Extensive promoter-centered chromatin interactions provide a topological basis for transcription regulation. *Cell* **148**, 84–98 (2012).

60. Kvon, E. Z. et al. Genome-scale functional characterization of *Drosophila* developmental enhancers in vivo. *Nature* **512**, 91–95 (2014).

61. Calhoun, V. C., Stathopoulos, A. & Levine, M. Promoter-proximal tethering elements regulate enhancer–promoter specificity in the *Drosophila Antennapedia* complex. *Proc. Natl Acad. Sci. USA* **99**, 9243–9247 (2002).

62. Ringel, A. R. et al. Repression and 3D-restructuring resolves regulatory conflicts in evolutionarily rearranged genomes. *Cell* **185**, 3689–3704 (2022).

63. Juven-Gershon, T. & Kadonaga, J. T. Regulation of gene expression via the core promoter and the basal transcriptional machinery. *Dev. Biol.* **339**, 225–229 (2010).

64. Zabidi, M. A. et al. Enhancer–core-promoter specificity separates developmental and housekeeping gene regulation. *Nature* **518**, 556–559 (2014).

65. Bergman, D. T. et al. Compatibility rules of human enhancer and promoter sequences. *Nature* **607**, 176–184 (2022).

66. Martinez-Ara, M., Comoglio, F., van Arensbergen, J. & van Steensel, B. Systematic analysis of intrinsic enhancer–promoter compatibility in the mouse genome. *Mol. Cell* **82**, 2519–2531 (2022).

67. Batut, P. J. et al. Genome organization controls transcriptional dynamics during development. *Science* **375**, 566–570 (2022).

68. Pachano, T. et al. Orphan CpG islands amplify poised enhancer regulatory activity and determine target gene responsiveness. *Nat. Genet.* **53**, 1036–1049 (2021).

69. Galouzis, C. C. & Furlong, E. E. M. Regulating specificity in enhancer–promoter communication. *Curr. Opin. Cell Biol.* **75**, 102065 (2022).

70. Chakraborty, S. et al. Enhancer–promoter interactions can bypass CTCF-mediated boundaries and contribute to phenotypic robustness. *Nat. Genet.* **55**, 280–290 (2023).

71. Hung, T.-C., Kingsley, D. M. & Boettiger, A. N. Boundary stacking interactions enable cross-TAD enhancer–promoter communication during limb development. *Nat. Genet.* **56**, 306–314 (2024).

72. Jiang, Y. et al. The methyltransferase SETDB1 regulates a large neuron-specific topological chromatin domain. *Nat. Genet.* **49**, 1239–1250 (2017).

73. Wang, Y. et al. The 3D Genome Browser: a web-based browser for visualizing 3D genome organization and long-range chromatin interactions. *Genome Biol.* **19**, 151 (2018).

74. ENCODE Project Consortium. An integrated encyclopedia of DNA elements in the human genome. *Nature* **489**, 57–74 (2012).

75. Amândio, A. R. et al. Sequential in *cis* mutagenesis in vivo reveals various functions for CTCF sites at the mouse *HoxD* cluster. *Genes Dev.* **35**, 1490–1509 (2021).

76. Flöttmann, R. et al. Noncoding copy-number variations are associated with congenital limb malformation. *Genet. Med.* **20**, 599–607 (2018).

77. Short, P. J. et al. De novo mutations in regulatory elements in neurodevelopmental disorders. *Nature* **555**, 611–616 (2018).

78. Firth, H. V. et al. DECIPHER: database of chromosomal imbalance and phenotype in humans using Ensembl resources. *Am. J. Hum. Genet.* **84**, 524–533 (2009).

79. ENCODE Project Consortium et al. Expanded encyclopaedias of DNA elements in the human and mouse genomes. *Nature* **583**, 699–710 (2020).

Methods

Ethics statement

All animal work was reviewed and approved by the Lawrence Berkeley National Laboratory Animal Welfare and Research Committee and the University of California Irvine Laboratory Animal Resources under protocols AUP-20-001 and AUP-23-005. Mice were housed in the animal facility, where their conditions were electronically monitored 24/7 with daily visual checks by technicians.

Tissue collection

Mouse embryonic tissues, including the forebrain, midbrain, hindbrain, neural tube, tail, facial mesenchyme, forelimb, hindlimb, heart and trunk, were collected from FVB/NCrl strain *Mus musculus* animals (Charles River). Wild-type male and female mice were mated using a standard timed breeding strategy, and embryos at E11.5 were collected for dissection using approved institutional protocols. Embryos were excluded if they were not at the expected developmental stage. Only one embryonic litter was processed at a time, and tissues and embryos were kept on ice to avoid degradation during tissue collection. Tissue from multiple embryos was pooled together in the same collection tube, and at least two separate tubes were collected for each tissue for biological replication.

Tissue processing for the Hi-C library

To prepare nuclei for constructing the Hi-C library, tissues were incubated with collagenase (Gibco) in a thermomixer at 37 °C until cells were dissociated, about 10–20 min. Cells were fixed by adding formaldehyde (Sigma-Aldrich) to a final concentration of 2% at room temperature for 10 min[41,80]. Ice-cold glycine solution was added to a final concentration of 200 mM to quench cross-linking. Cells were then resuspended in cold lysis buffer (50 mM Tris, pH 7.5, 150 mM NaCl, 5 mM EDTA, 0.5% NP-40, 1.15% Triton X-100 and 1× protease inhibitor cocktail (Thermo Scientific)) and incubated on ice for 15 min. Pellets of nuclei were obtained by centrifugation at 750g for 5 min at 4 °C, followed by snap freezing and storage at −80 °C.

Generation of Hi-C libraries

Hi-C libraries were prepared as described previously[80–82]. Briefly, frozen nuclear pellets (2–6 million) were thawed on ice, followed by adding SDS and Triton X-100 to remove noncross-linked proteins and sequester SDS, and digested using DpnII (NEB) overnight at 37 °C. The ends of restriction fragments were labeled with biotinylated dCTP and ligated at room temperature for 4 h. After decross-linking and precipitation, ligated products were sheared using a Covaris sonicator (duty cycle, 10%; intensity, 5; cycles per burst, 200; treatment time, 180 s in total) to an average fragment size of 200 bp. The ligated sheared 3C libraries (10–12 µg for each replicate) were pulled down using streptavidin Dynabeads (Thermo Scientific) to eliminate unligated fragments, followed by end repair, adaptor ligation and library amplification according to the modified Agilent SureSelectXT protocol.

Capture Hi-C probe design

To perform enhancer capture Hi-C, we designed 120-mer RNA probes, targeting 935 enhancer regions that showed highly reproducible activity at E11.5 from the VISTA Enhancer database[83] (Supplementary Table 1). We also designed RNA probes targeting 176 promoters and 87 elements with no reproducible enhancer activity at E11.5 as negative controls (Supplementary Table 1). All elements shorter than 2 kb were resized to 2 kb (±1 kb from their central coordinate).

We designed 20,452 120-mer probes (each region was covered by, on average, 17 RNA probes) using the following pipeline. We first identified the DpnII restriction sites (GATC) overlapping each element by generating a genome-wide map of cut sites using Vmatch (http://www.vmatch.de/). For each of the DpnII restriction sites overlapping the resized VISTA elements, ±240 bp around the recognition site was

considered for tiling. Among the resulting regions, those found within 60 bp of each other were further merged. After that, these regions were tiled (from −60 bp to +60 bp) using overlapping 120-bp windows, with a step of 60 bp. The obtained tiles were further filtered based on their overlap with repetitive elements and their predicted mappability using short reads. For filtering based on mappability, the 'wgEncodeCrgMapabilityAlign36mer.bigWig' track from the UCSC genome browser (mm9) was used. Only tiles showing a mappability score of 1 across all 120 bp were retained. For exclusion based on repeats, the tiles were first lifted to mm10 (using liftOver), and then each tile showing an overlap of at least 10% with an annotated repeat in the RepeatMasker track of the UCSC genome browser was excluded. Following that, only those overlapping elements represented by at least three tiles were considered for the final design. For capture Hi-C experiments at the *Shh*–ZRS locus (Fig. 6), we designed a separate panel that covered the ZRS enhancer, part of the bacterial *lacZ* sequence and nine control regions (Supplementary Table 1).

Capture Hi-C library construction and sequencing

The enhancer capture Hi-C library was created by performing a target-enrichment protocol using capture RNA probes according to the Agilent SureSelectXT protocol with an input amount of 750 ng of the Hi-C library per sample. Following hybridization to the RNA oligonucleotide library, each capture Hi-C library was sequenced (paired-end 100 or 150 bp) to enrich enhancer-centric interactions, yielding a total of 1 billion unique paired-end reads.

Capture Hi-C data analysis

After checking read quality with FastQC (version 0.11.9), ligated reads were trimmed using DpnII restriction recognition sites and mapped to the DpnII-digested reference genome (mm10) using HiCUP (version 0.8.0)[84], followed by quality filtering and deduplication. For each tissue, the capture Hi-C experiment produced, on average, 20 million unique on-target paired-end reads, resulting in a total of 200 million valid read pairs (Supplementary Table 1).

Next, all DpnII fragments overlapping with the same bait region were merged into a single fragment in silico. Subsequently, the rest of the DpnII fragments were merged based on the size distribution of the pooled fragments that overlapped with bait regions. The mean fragment size of pooled fragments was ~3,000 bp. Significant interactions were called with CHiCAGO (version 1.26.0, score > 5) using the default setting[85,86] and combined replicates from the HiCUP pipeline by using the design file with the following parameters: '−minFragLen=300 −maxFragLen=20000 −binsize=20000 −maxLBrownEst=3000000 −removeAdjacent=FALSE'. We removed significant interactions that did not have valid di-tag reads on neighboring fragments to avoid spurious interaction spikes[87]. Interactions called >2 Mb from the bait regions were excluded from the downstream analysis.

To visualize and compare interaction frequencies between different tissues, read counts were normalized across ten tissues with Chicdiff (version 0.6)[86,88] to account for library size and background differences between samples. We used the output from CHiCAGO to make a peak matrix and performed the normalization in Chicdiff with the following setting parameters: 'norm="fullmean", Score=3, RUexpand=3L'. Di-tag reads between different bait regions were removed from the analysis.

For the classification of enhancer-interacting regions in Extended Data Fig. 1d, we used promoter annotations from the latest version of the Ensembl Regulatory Build[89], CTCF-binding sites at E12.5 from publicly available data (GSE181383)[75], putative enhancers based on H3K27ac occupancy (from E10.5 to E12.5) and polycomb-associated H3K27me3-marked regions (at E10.5–E12.5) from the ENCODE database[79]. We further filtered promoters by only keeping those within ±2.5 kb around TSSs that were transcribed (TPM > 0.5 from RNA-seq data in the ENCODE database) in at least one of the following embryonic

stages: E10.5, E11.5 and E12.5. CTCF sites were divided into two categories based on whether they were within a TAD or at a TAD boundary. Overlaps of interaction peaks with promoters, CTCF sites, enhancers and polycomb regions were computed sequentially, which means that peaks were assigned to only one category, and by extending the interaction peaks by ±5 kb.

For the E–P interaction analysis in Figs. 2, 4 and 6 and Extended Data Figs. 6 and 7, we focused on 969 E–P interactions in which the enhancer and interacting gene were both active in at least one tissue. To construct the metaplot profile in Fig. 4, interaction frequencies were scaled as follows: (1) the 5' end (10 kb around the midpoint of the baited enhancer) and the 3' end (10 kb around the midpoint of interacting promoters) were unscaled; (2) the regions between them have been scaled to 100 kb. Light blue shading indicates 95% confidence intervals estimated by nonparametric bootstrapping. The in vivo enhancer rank used in Extended Data Figs. 6f and 8c is based on a metric that combines the reproducibility, strength and specificity of staining in the structure(s) of interest and was determined by multiple annotators blinded to genotype (1, worst; 5, best)[27].

To perform k-means clustering for the E–P interactions in Fig. 4a, normalized interaction frequencies were scaled to the maximum value among ten tissues, and clustering was performed in R (version 4.1.2) with $k = 10$ and 'nstart=30'. Clusters were ordered using 'hclust()' with the 'ward.D' method and visualized using the clusterProfiler (version 3.0.4) package[90,91].

For DNA methylation and DNase signal comparison for interacting and skipped genes in Fig. 2 and Extended Data Fig. 4a–c, we counted the read counts ±1 kb around the TSS of each gene for every enhancer–gene interaction. For comparison to H3K27me3 and H3K9me3 regions, we extended the region analyzed to ±2.5 kb of sequence around the TSS of each gene. For CpG island length analyses in Extended Data Fig. 4g, data were downloaded from the UCSC browser (http://genome.ucsc.edu/cgi-bin/hgTrackUi?g=cpgIslandExt). The differences between interacting and skipped genes were calculated by nonparametric Wilcoxon–Mann–Whitney tests, except for the comparison for the fraction of promoters marked with H3K27me3, which was calculated using the χ^2 test.

For E–E interaction analysis in Fig. 4 and Extended Data Fig. 8, we overlapped enhancer interactions with H3K27ac peaks in the corresponding tissues in embryos at E11.5 (signal > 5).

Generation of enhancer-knockout and -knockin mice

Enhancer-knockout mice were created using a modified CRISPR–Cas9 protocol[32,92]. Briefly, pronuclei of FVB mouse zygotes were injected with a mix of Cas9 protein (final concentration of 20 ng µl⁻¹, IDT) and sgRNA species targeting enhancer regions (50 ng µl⁻¹) (Extended Data Fig. 5). To replace the ZRS with the fragment of the *lacZ* sequence, we used a previously described strategy[31]. Briefly, pronuclei of FVB mouse zygotes were injected with Cas9 protein, a donor plasmid (25 ng µl⁻¹) containing a fragment of the bacterial *lacZ* sequence and homology arms and sgRNA targeting the ZRS region Cas9 protein[31] (Extended Data Fig. 9). F₀ mice were genotyped by PCR and Sanger sequencing using the primers in Supplementary Table 5.

In situ hybridization

WISH was employed as previously described[31] to detect *Shh* expression in mouse embryos using digoxigenin-labeled antisense riboprobes (Supplementary Table 5) and synthesized in vitro from a linearized plasmid using RNA Labeling Mix (Roche) and T3 RNA polymerase (Roche). Embryos were fixed with 4% paraformaldehyde (PFA), cleansed in PBT (PBS with 0.1% Tween-20), dehydrated through a methanol series and preserved at −20 °C in 100% methanol. For ISH, the embryos were rehydrated, bleached with 6% H₂O₂–PBT for 15 min and treated with 10 mg ml⁻¹ proteinase K in PBT for 20 min. After proteinase K permeabilization, the embryos were incubated in 2 mg ml⁻¹ glycine

in PBT, rinsed twice with PBT and post-fixed with 0.2% glutaraldehyde–4% PFA in PBT for 20 min. After three PBT washes, the embryos were transferred to prehybridization buffer (50% deionized formamide, 5× SSC, pH 4.5, 2% Roche Blocking Reagent, 0.1% Tween-20, 0.5% CHAPS, 50 mg ml⁻¹ yeast RNA, 5 mM EDTA, 50 mg ml⁻¹ heparin) for an hour at 70 °C, which was after replaced with hybridization buffer containing 1 mg ml⁻¹ Dig-labeled riboprobe for overnight incubation at 70 °C with gentle rotation. The following day, post-hybridization washes were performed at 70 °C for 5 min with increasing concentrations of 2× SSC, pH 4.5, starting from 100% prehybridization buffer, 75% prehybridization buffer–25% 2× SSC, 50% prehybridization buffer–50% 2× SSC, 25% prehybridization buffer–75% 2× SSC, followed by 2× SCC, 0.1% CHAPS twice for 30 min at 70 °C with gentle rotation. The embryos were then treated with 20 mg ml⁻¹ RNase A in 2× SSC, 0.1% CHAPS for 45 min at 37 °C, followed by two 10-min washes in maleic acid buffer (100 mM maleic acid disodium salt hydrate, 150 mM NaCl, pH 7.5) at room temperature and two additional 30-min washes at 70 °C. Samples were then extensively washed with TBST (140 mM NaCl, 2.7 mM KCl, 25 mM Tris-HCl, 1% Tween-20, pH 7.5), blocked with 10% lamb serum–TBST for an hour and incubated overnight at 4 °C with anti-Dig-AP antibody (Roche, 1:5,000) in 1% lamb serum. Excess antibody was removed by washing the embryos with TBST (3×, 5 min), followed by five 1-h TBST washes and an overnight TBST incubation at 4 °C. The next morning, embryos were balanced in NTMT (100 mM NaCl, 100 mM Tris-HCl, 50 mM MgCl₂, 1% Tween-20, pH 9.5), and alkaline phosphatase activity was visualized by incubating in BM purple reagent (Roche) in the dark with gentle agitation. The reaction was stopped with five 10-min PBT washes. ISH-treated samples were stored long-term in 4% PFA–PBS and imaged with a Flexacam C1 camera mounted on a Leica M125C stereomicroscope.

RNA-seq data generation and analysis

Dissected tissues were immediately submerged in RNAprotect Tissue Reagent (Qiagen) and stored at −80 °C. Multiple samples from the same tissue and genotype were pooled into at least 1 million cells for each of the two replicates. RNA isolation, preparation of the RNA library and transcriptome sequencing was conducted by Novogene. All RNA-seq experiments were performed in biological replicates. Paired-end reads were mapped to the reference genome (mm10) using STAR (version 2.7.9a) software with default parameters[93] and were counted on RefSeq genes by HTSeq[94]. Differential gene expression analysis was performed using DESeq2 (version 3.16)[95]. Genes with adjusted P value < 0.05 were considered differentially expressed.

DNA fluorescence in situ hybridization in mouse embryonic tissues

DNA 3D-FISH was adapted from previously established methods[96–98]. Fosmid clones from the WIBR-1 library were purchased from the BACPAC Resources Center (for coordinates and names, see Supplementary Table 4) and isolated using the Large-Construct Kit (Qiagen).

Fluorescent probes were generated using the Nick translation DNA labeling system 2.0 (Enzo) with XFD 488-dUTP or Cyanine-3-dUTP (AAT Bioquest). Unincorporated nucleotides were removed using the QIAquick PCR Purification Kit (Qiagen). Probe size (50–500 bp) was analyzed by agarose gel electrophoresis, and the incorporation rate was assessed with the DeNovix DS-11 spectrophotometer[99]. Probes were then precipitated with 20× Mouse Cot-1 DNA (Invitrogen) and 20× Salmon Sperm DNA (Invitrogen) and resuspended at 100 ng µl⁻¹ in TE buffer.

Tissues (forelimb, forebrain, midbrain and face) were microdissected from mouse embryos at E11.5 and dissociated into single-cell suspensions through intubation at 37 °C in PBS with collagenase. Cell suspensions (50 µl, at approximately 5 × 10⁵ cells per ml) were dropped onto Poly-L-Lysine Coated Slides (Boster Bio) and incubated for 30 min at 37 °C in a humidity chamber. Slides were then incubated in ice-cold PBS and CSK buffer with 0.5% Triton X-100 for 5 min, respectively, and

then fixed in 4% PFA for 10 min. Slides were sequentially dehydrated in 70%, 80% and 100% ethanol, air dried and then treated with 400 µg ml⁻¹ RNase A (Fisher Scientific) for 30 min at 37 °C in a humidity chamber. Next, slides were washed with PBS before 10 min of incubation in 0.1 N HCl with 0.5% Tween-20 and 5 min in quenching PBS with 0.02% Tween-20. Samples were then denatured in 70% formamide in 2× SSC, pH 7.4 at 80 °C for 6 min and then dehydrated with 70%, 80% and 100% ethanol sequentially and air dried. Probes (100 ng) were diluted in 10 µl hybridization buffer, denatured at 80 °C for 10 min and pre-annealed for 30–90 min at 37 °C. Pre-annealed probes were added to the cells and covered with a coverslip. Hybridization was carried out in a humidity chamber at 37 °C for 16–18 h. On the next day, slides were washed with 50% formamide in 2× SSC three times, 2× SSC three times and then 0.1× SSC twice at 37 °C. Slides were then air dried and mounted in 8 µl VECTASHIELD Mounting Medium with DAPI (Vector Laboratories)

Image acquisition and analysis

Images were obtained on a Zeiss LSM 900 Airyscan 2 using a ×63 oil objective and an Axiocam 503 mono camera. Lasers were set at 405-nm (DAPI channel, 3.5% power, 800 V of gain, 0 offset), 488-nm (488 enhancer probe channel, 4.0% power, 800 V of gain, 0 offset) and 561-nm (Cy3 promoter probe channel, 4.0% power, 750 V of gain, 0 offset) laser lines, and emission bandpass was set at 400/502 nm (DAPI channel), 496/566 nm (488 probe channel) and 560/700 nm (Cy3 probe channel). SR-4Y multiplex acquisition with a scan speed of 8 was used with a pixel time of 0.5 µs and a pixel size of 0.04 µm; pinhole size was set at 0.2 Airy units. Z stacks of ten slices spanning the nucleus (as determined by the DAPI channel) were taken, resulting in an average step size of 0.5 µm. Images were deconvoluted using ZEN Blue Software (Zeiss) Airyscan 2 to produce 3D images, and the resulting 3D images were analyzed using Imaris software (Oxford Instruments). We used the Spots module (threshold was set automatically by the software) to computationally identify FISH probe foci. Only foci within the DAPI-stained area containing single probe signals were analyzed to eliminate sister chromatids. The centroids of foci were modeled using PSF elongation along the z axis to create elliptical-shaped spots. Interprobe distances were automatically calculated as the distance in 3D between the centroids of the 488 and Cy3 probe foci. The object-to-object statistics module was used to identify the closest Cy3 promoter focus to each 488 enhancer focus and calculate promoter–enhancer distances. Only pairs with a distance <1.5 µm were considered for further analysis.

Statistics and reproducibility

No prior analyses were used to determine sample size before the experiment. Embryos that were not at the correct developmental stage were excluded from data collection. For DNA FISH image analysis, only alleles within the DAPI-stained area and with single probe signals were analyzed to eliminate sister chromatids. Interprobe distances were measured with the closest distance between a pair of probes, and only distances <1.5 µm were considered. For the capture Hi-C and RNA-seq experiment, wild-type, knockin and knockout littermates were randomized and identified only by numbers, with genotype unknown to the investigator during data collection and sample processing. For each tissue and corresponding probe set for DNA FISH, random x−y coordinates were selected, and a 9 × 9 tiled image was taken. For RNA-seq, investigators were blinded to animals' genotypes during sample collection and library preparation for the two knockout lines generated in this study. For ISH experiments in knockin embryos, investigators were blinded to animals' genotypes during tissue collection and in situ hybridization. For capture Hi-C experiments, blinding was not performed because all metrics were derived from absolute quantitative measurements without human subjectivity. For DNA FISH, after manual data exclusion (see above), focus recognition and distance measurement was carried out with an automated algorithm (Imaris).

For comparison of interaction frequencies, histone modifications, DNase accessibility or interprobe distances for 3D DNA FISH, no assumptions of normality were made, and all tests were performed using the nonparametric Wilcoxon–Mann–Whitney test, the nonparametric Fisher's exact test or the χ^2 test. Wilcoxon–Mann–Whitney tests were performed in R using 'wilcox.test()' as a two-sided test. Detailed statistical analyses used in the paper are described in the Methods. Statistical tests were chosen as appropriate for the data types as described.

Reporting summary

Further information on research design is available in the Nature Portfolio Reporting Summary linked to this article.

Data availability

Sequencing data generated in this study are available at the Gene Expression Omnibus repository under accession number GSE217078. Several mouse embryonic ChIP–seq, DNase-seq, bisulfite-seq and RNA-seq data for different tissues at E11.5 were downloaded from ENCODE (https://www.encodeproject.org/). The CTCF ChIP–seq datasets used for comparison were downloaded from GEO (https://www.ncbi.nlm.nih.gov/geo/) under accession numbers GSM5501396, GSM5501397 and GSM5501398. Enhancer interaction profiles are available at https://www.kvonlab.org/data/echic. Source data are provided with this paper.

Code availability

Public software and packages were used following the developer's manuals. The custom code used for data analysis has been deposited at GitHub (https://github.com/kvonlab/Chen_et_al_2024) and Zenodo (https://doi.org/10.5281/zenodo.10594800)[100].

References

80. Dryden, N. H. et al. Unbiased analysis of potential targets of breast cancer susceptibility loci by capture Hi-C. *Genome Res.* **24**, 1854–1868 (2014).
81. Hughes, J. R. et al. Analysis of hundreds of *cis*-regulatory landscapes at high resolution in a single, high-throughput experiment. *Nat. Genet.* **46**, 205–212 (2014).
82. Orlando, G., Kinnersley, B. & Houlston, R. S. Capture Hi-C library generation and analysis to detect chromatin interactions. *Curr. Protoc. Hum. Genet.* **98**, e63 (2018).
83. Pennacchio, L. A. et al. In vivo enhancer analysis of human conserved non-coding sequences. *Nature* **444**, 499–502 (2006).
84. Wingett, S. et al. HiCUP: pipeline for mapping and processing Hi-C data. *F1000Res.* **4**, 1310 (2015).
85. Cairns, J. et al. CHiCAGO: robust detection of DNA looping interactions in capture Hi-C data. *Genome Biol.* **17**, 127 (2016).
86. Freire-Pritchett, P. et al. Detecting chromosomal interactions in capture Hi-C data with CHiCAGO and companion tools. *Nat. Protoc.* **16**, 4144–4176 (2021).
87. Schoenfelder, S. et al. The pluripotent regulatory circuitry connecting promoters to their long-range interacting elements. *Genome Res.* **25**, 582–597 (2015).
88. Cairns, J., Orchard, W. R., Malysheva, V. & Spivakov, M. Chicdiff: a computational pipeline for detecting differential chromosomal interactions in capture Hi-C data. *Bioinformatics* **35**, 4764–4766 (2019).
89. Zerbino, D. R., Wilder, S. P., Johnson, N., Juettemann, T. & Flicek, P. R. The Ensembl Regulatory Build. *Genome Biol.* **16**, 56 (2015).
90. Yu, G., Wang, L.-G., Han, Y. & He, Q.-Y. clusterProfiler: an R package for comparing biological themes among gene clusters. *OMICS* **16**, 284–287 (2012).
91. Wu, T. et al. clusterProfiler 4.0: a universal enrichment tool for interpreting omics data. *Innovation* **2**, 100141 (2021).

92. Osterwalder, M. et al. Characterization of mammalian in vivo enhancers using mouse transgenesis and CRISPR genome editing. *Methods Mol. Biol.* **2403**, 147–186 (2022).

93. Dobin, A. et al. STAR: ultrafast universal RNA-seq aligner. *Bioinformatics* **29**, 15–21 (2013).

94. Putri, G. H., Anders, S., Pyl, P. T., Pimanda, J. E. & Zanini, F. Analysing high-throughput sequencing data in Python with HTSeq 2.0. *Bioinformatics* **38**, 2943–2945 (2022).

95. Love, M. I., Huber, W. & Anders, S. Moderated estimation of fold change and dispersion for RNA-seq data with DESeq2. *Genome Biol.* **15**, 550 (2014).

96. Chaumeil, J., Micsinai, M. & Skok, J. A. Combined immunofluorescence and DNA FISH on 3D-preserved interphase nuclei to study changes in 3D nuclear organization. *J. Vis. Exp.* **3**, e50087 (2013).

97. Naciri, I. et al. Linking chromosomal silencing with *Xist* expression from autosomal integrated transgenes. *Front. Cell Dev. Biol.* **9**, 693154 (2021).

98. Chaumeil, J., Augui, S., Chow, J. C. & Heard, E. Combined immunofluorescence, RNA fluorescent in situ hybridization, and DNA fluorescent in situ hybridization to study chromatin changes, transcriptional activity, nuclear organization, and X-chromosome inactivation. *Methods Mol. Biol.* **463**, 297–308 (2008).

99. Bolland, D. J., King, M. R., Reik, W., Corcoran, A. E. & Krueger, C. Robust 3D DNA FISH using directly labeled probes. *J. Vis. Exp.* https://doi.org/10.3791/50587 (2013).

100. Chen, Z. & Kvon, E. Z. Analysis pipeline for Chen_et_al_2024 paper. *Zenodo* https://doi.org/10.5281/zenodo.10594800 (2024).

101. Kvon, E. Z. et al. Comprehensive in vivo interrogation reveals phenotypic impact of human enhancer variants. *Cell* **180**, 1262–1271 (2020).

102. Uslu, V. V. et al. Long-range enhancers regulating Myc expression are required for normal facial morphogenesis. *Nat. Genet.* **46**, 753–758 (2014).

103. Padhi, E. M. et al. Coding and noncoding variants in *EBF3* are involved in HADDS and simplex autism. *Hum. Genomics* **15**, 44 (2021).

104. Turner, T. N. et al. Genomic patterns of de novo mutation in simplex autism. *Cell* **171**, 710–722 (2017).

105. Shibata, M., Kurokawa, D., Nakao, H., Ohmura, T. & Aizawa, S. MicroRNA-9 modulates Cajal–Retzius cell differentiation by suppressing Foxg1 expression in mouse medial pallium. *J. Neurosci.* **28**, 10415–10421 (2008).

106. Shimogori, T. et al. A genomic atlas of mouse hypothalamic development. *Nat. Neurosci.* **13**, 767–775 (2010).

107. Rodríguez-Carballo, E. et al. The *HoxD* cluster is a dynamic and resilient TAD boundary controlling the segregation of antagonistic regulatory landscapes. *Genes Dev.* **31**, 2264–2281 (2017).

Author contributions

E.Z.K. conceived the project with input from Z.C., V.S., D.E.D., A.V. and L.A.P. Z.C., V.S., I.B. and E.Z.K. designed experiments. Z.C., V.S., G.B., S.J., B.C. and E.Z.K. performed capture Hi-C experiments, and Z.C. analyzed the data with input from E.Z.K. and B.J.M. Z.C., S.J., A.D. and E.Z.K. performed enhancer-knockout studies, and Z.C. analyzed the data. Z.C. and G.B. performed 3D-FISH experiments and analyzed the data. A.A.-C. and J.L.-R. performed ISH experiments. E.Z.K and Z.C. wrote the paper with input from the remaining authors.

Competing interests

The authors declare no competing interests.

Additional information

Extended data is available for this paper at https://doi.org/10.1038/s41588-024-01681-2.

Supplementary information The online version contains supplementary material available at https://doi.org/10.1038/s41588-024-01681-2.

Correspondence and requests for materials should be addressed to Evgeny Z. Kvon.

Peer review information *Nature Genetics* thanks Daniel Ibrahim, Douglas Higgs and the other, anonymous, reviewer(s) for their contribution to the peer review of this work.

Reprints and permissions information is available at www.nature.com/reprints.
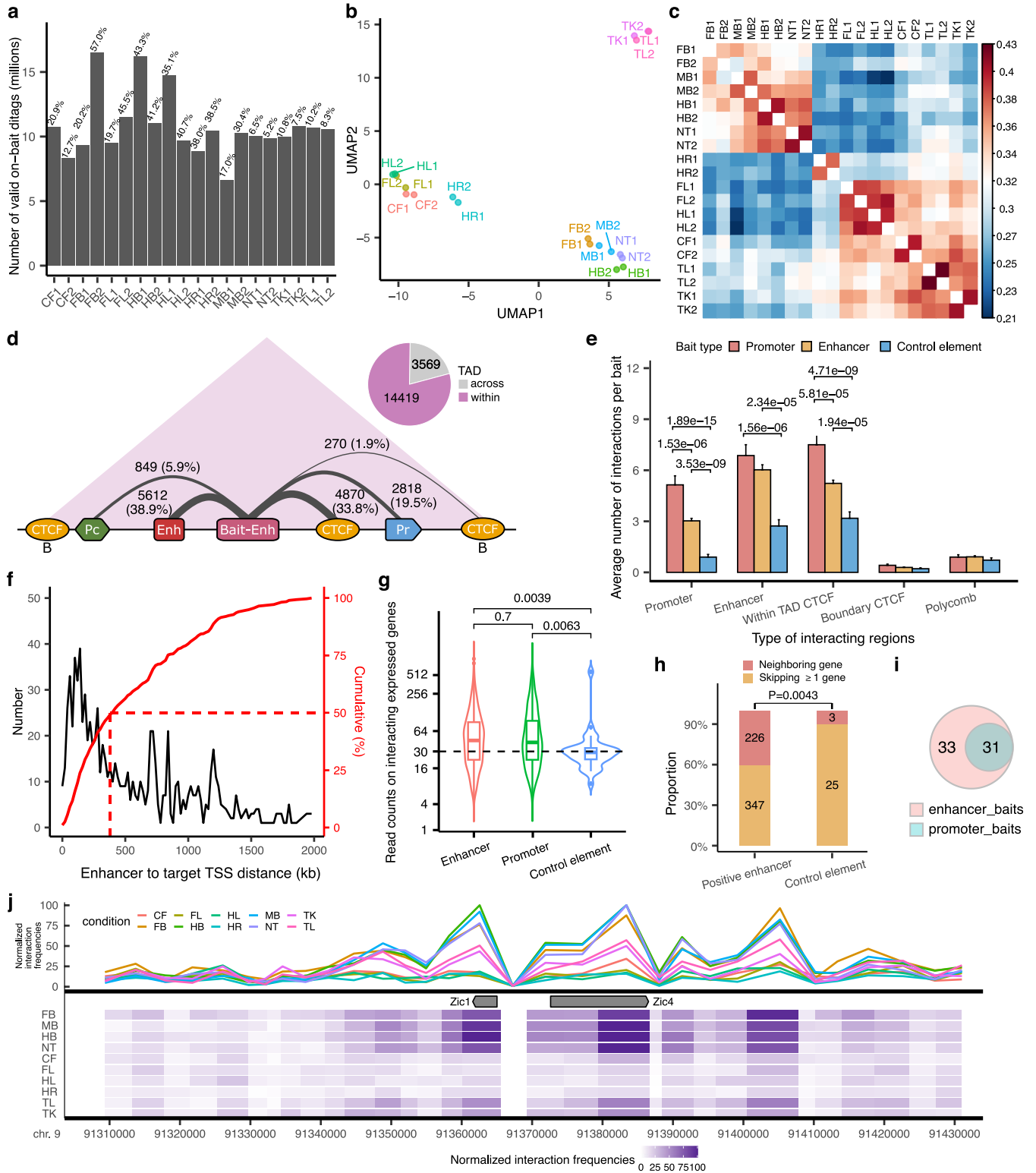
Extended Data Fig. 1 | See next page for caption.

Extended Data Fig. 1 | Enhancer capture Hi-C identifies enhancer-centric chromatin interactions in mouse embryonic tissues. a, Unique on-target read counts for each library. The percentages above indicate the capture rates for each library. **b**, **c**, Principal component analysis and hierarchical clustering of all replicates based on the presence of peaks called by CHiCAGO in each replicate (considering peaks with valid di-tags on neighboring fragments). **d**, Significant enhancer-centric chromatin interactions identified in this study. The number on each link represents the number of fragments falling into different annotation categories and the width of links is proportional to the percentage (in the parentheses) of different kinds of interactions. Only interactions within 2 Mb are included. CTCF sites with 'B': CTCF sites at TAD boundary; Pc: polycomb; Enh: enhancers; Bait-Enh: baited enhancers; Pr: promoters. **e**, An average number of interactions detected per bait for different kinds of baits (promoter (n = 176), enhancer (n = 935) and negative control elements (n = 87)). Data are represented as mean ± s.e.m. **f**, Distribution of genomic distances between enhancers and the TSSs of interacting genes (black, frequencies; red, cumulative). **g**, Violin plots showing read counts on promoters of active genes that interact with enhancer baits (n = 541), promoter baits (n = 126) and control element baits (n = 25). The central horizontal lines are the median, with the boxes extending from the 25th to the 75th percentiles. The whiskers further extend by ±1.5 times the interquartile range from the limits of each box. **h**, Histogram showing the proportion of bait regions that interact with proximal genes and distal genes. **i**, Venn diagram showing the overlap between significant interactions called from enhancer baits and corresponding promoter baits. All P values were calculated by a two-sided Wilcox test and adjusted for multiple testing. **j**, Zoom-in view on *Zic1/Zic4* locus for hs654 interaction profiles across 10 tissues. The average size for each pooled fragment is ~3 kb. FB, forebrain. MB, midbrain. HB, hindbrain. CF, face. HR, heart. FL, forelimb. HL, hindlimb. TK, trunk. TL, tail. NT, neural tube.
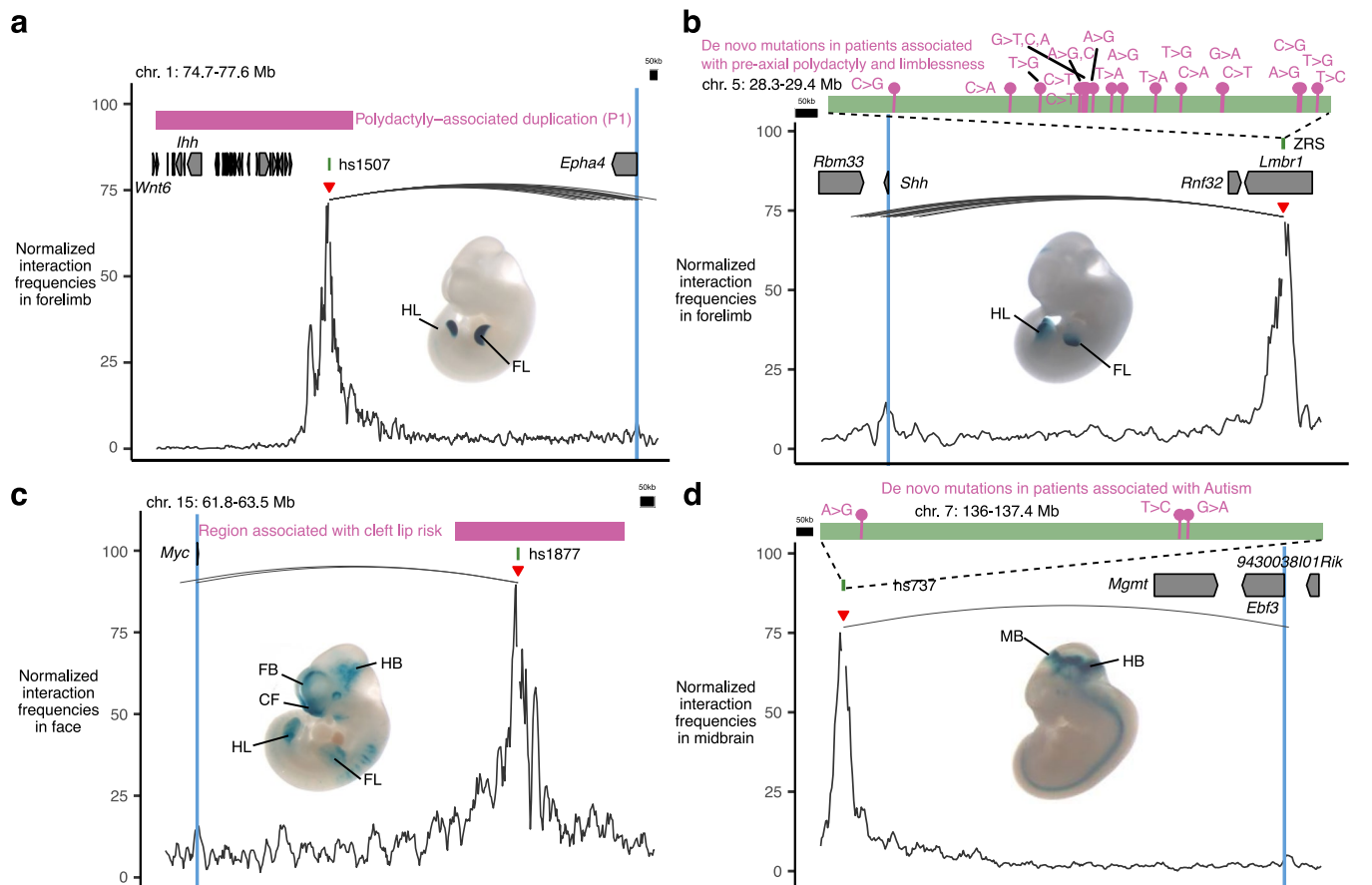
Extended Data Fig. 2 | Examples of enhancer–promoter interactions linked to congenital disorders. a, Hs1507 limb enhancer (green) located in the non-coding region which is duplicated in patients with polydactyly (pink bar indicates the homologous region in the mouse genome)[8]. Hs1507 forms significant chromatin interactions with the promoter of the *Epha4* (blue line) located ~1.5 Mb away. Shown is the *Epha4* genomic region (chr1:74,788,119-77,634,678; mm10). **b**, Many de novo rare variants identified in patients with preaxial polydactyly[101] are located in the ZRS limb enhancer (green bar) which forms significant interactions with the promoter of *Shh* located ~850 kb away. Shown is the *Shh* (blue line) genomic region (chr5:28,320,000-29,400,000; mm10). **c**, Hs1877

face enhancer (green) located in the non-coding region containing 146 SNPs found in patients with cleft lip risk (purple bar indicates the homologous region in the mouse genome)[102]. Hs1877 forms significant chromatin interactions with the promoter of the *Myc* (blue line) located ~900 kb away in the face. The *Myc* genomic region (chr15:61,880,003-63,506,895; mm10). **d**, Three de novo rare variants identified in patients with autism are located in the hs737 midbrain/hindbrain enhancer (green bar)[103,104], which forms strong significant interactions with the promoter of *Ebf3* (blue line) located ~1,000 kb away in the midbrain. Shown is the Ebf3 genomic region (chr7:136,018,204-137,420,338; mm10). Red arrowheads indicate capture Hi-C viewpoints.
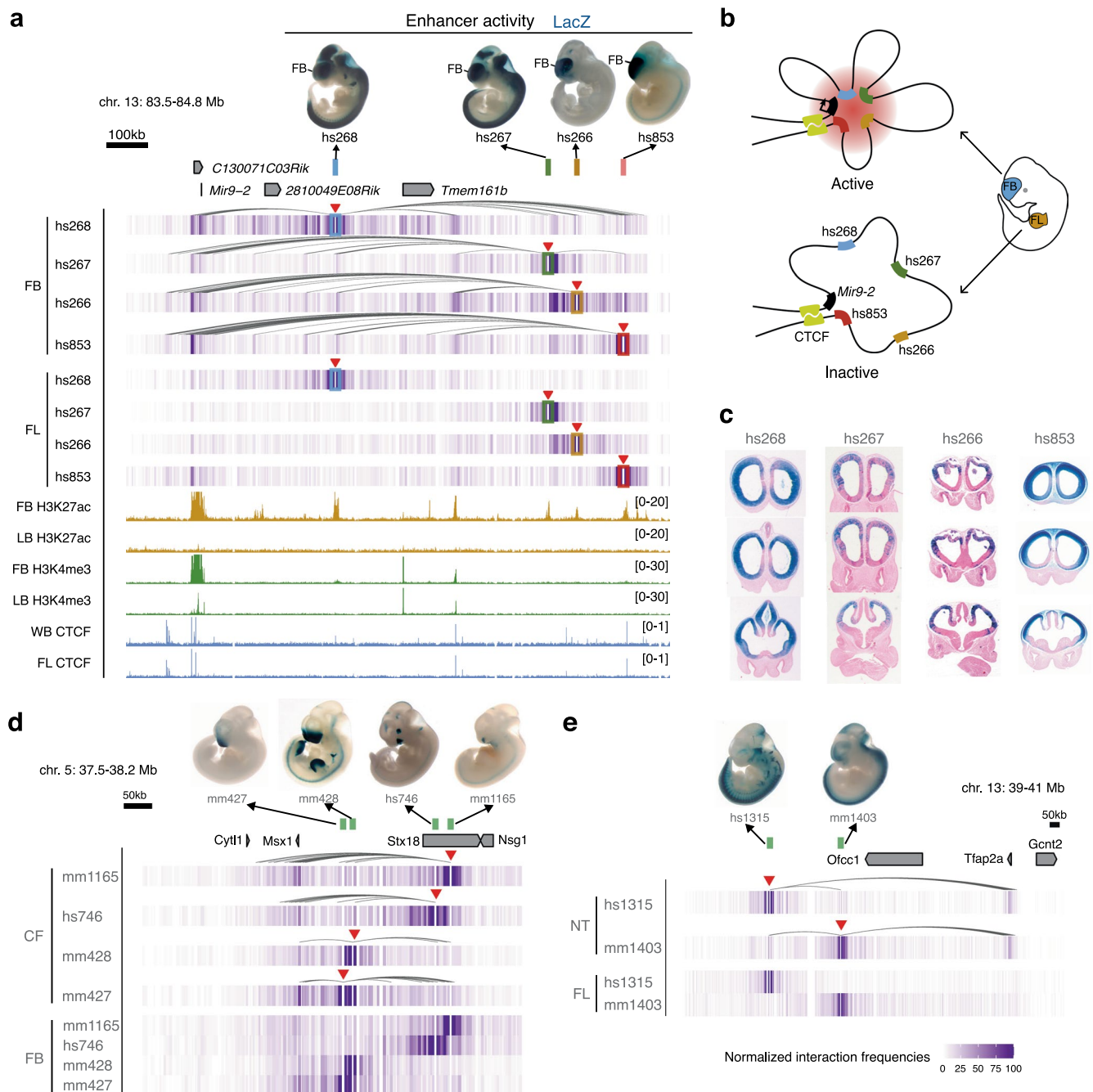
Extended Data Fig. 3 | Examples of enhancer−enhancer chromatin interactions. a, The *Mir9-2* genomic region (chr13:83,558,457-84,861,438; mm10) is shown with chromatin interaction heatmaps centered on hs268 (blue), hs267 (green), hs266 (yellow) and hs853 (red) enhancers in the forebrain (FB) and forelimb (FL). Shown on the top are hs268, hs267, hs266 and hs853 enhancer activities in a transgenic mid-gestation (E11.5) mouse embryo, which match with the expression profiles of *Mir9* in the brain and neural tube at E11.5[105,106]. Red arrowheads indicate capture Hi-C viewpoints. Arches indicate significant interactions in the forebrain. Shown on the bottom are H3K27ac (yellow) and H3K4me3 (green) ChIP-seq tracks in forebrain and limb buds (LB) at E11.5, CTCF (light blue) ChIP-seq tracks in the whole brain (WB) and forelimb at E12.5[33,74,75,107]. **b**, Schematic depicting 3D chromatin interactions between enhancers and *Mir9-2*
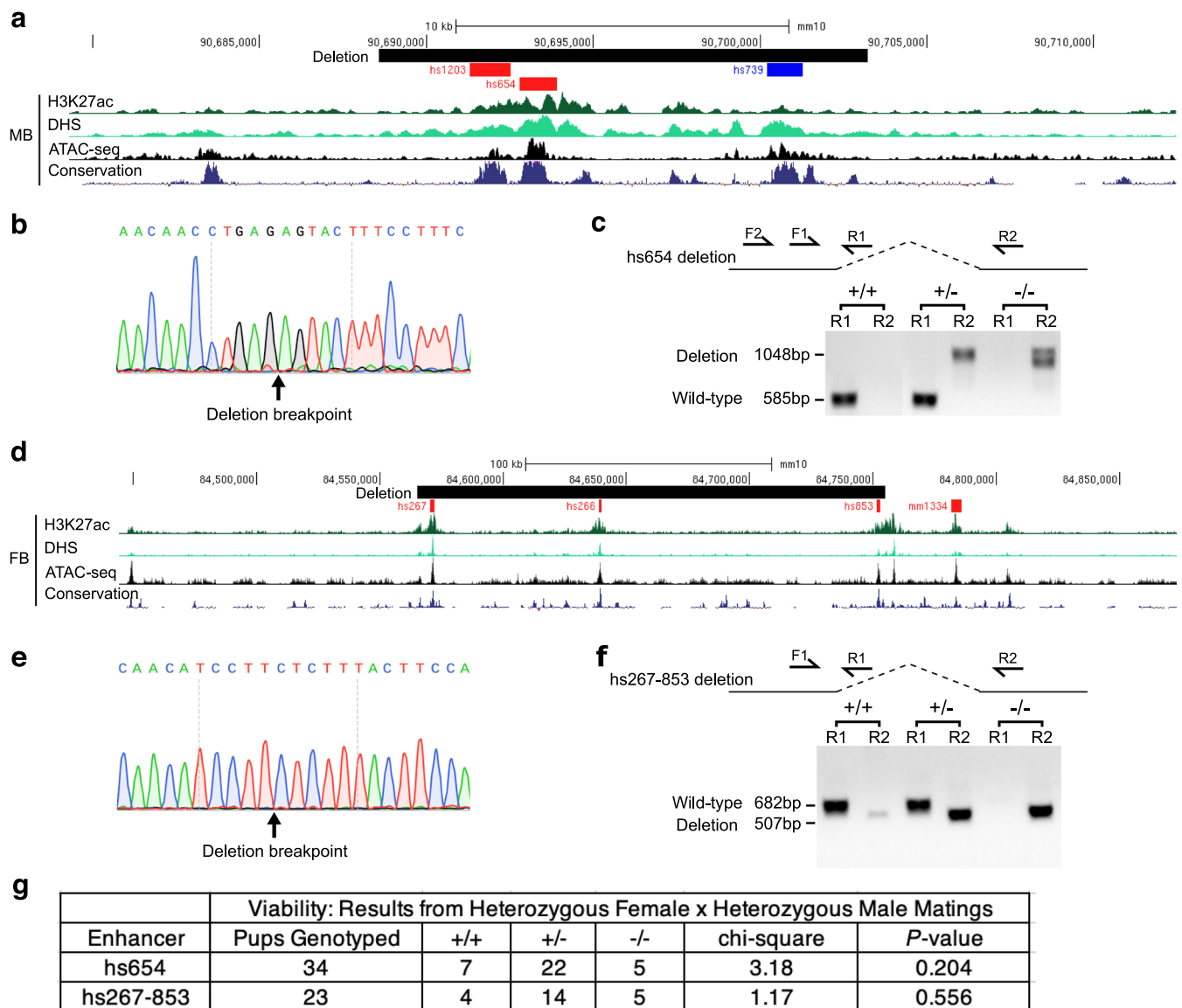
gene in the forebrain and forelimb. **c**, Coronal sections of forebrain for hs268, hs267, hs266 and hs853 enhancer activity from VISTA enhancer database[27], which reproducibly label the same subregions in E11.5 forebrain as *C130071C03Rik* (*Mir9-2* precursor) expression[106]. **d**, **e**, Chromatin interaction heatmaps centered on mm1165, hs746, mm428 and mm427 enhancers in the face (CF) and forebrain (FB) for *Msx1* genomic region (chr5: 37,554,764-38,206,723; mm10) (d) and hs1315 and mm1403 enhancers in the neural tube (NT) and forelimb (FL) for *Tfap2a* genomic region (chr13: 39,098,000-41,000,000; mm10) (e). Shown on the top are mm1165, hs746, mm428, mm427, hs1315 and mm1403 enhancer activities in a transgenic mid-gestation (E11.5) mouse embryos. Arches indicate significant interactions. Red arrowheads indicate capture Hi-C viewpoints.
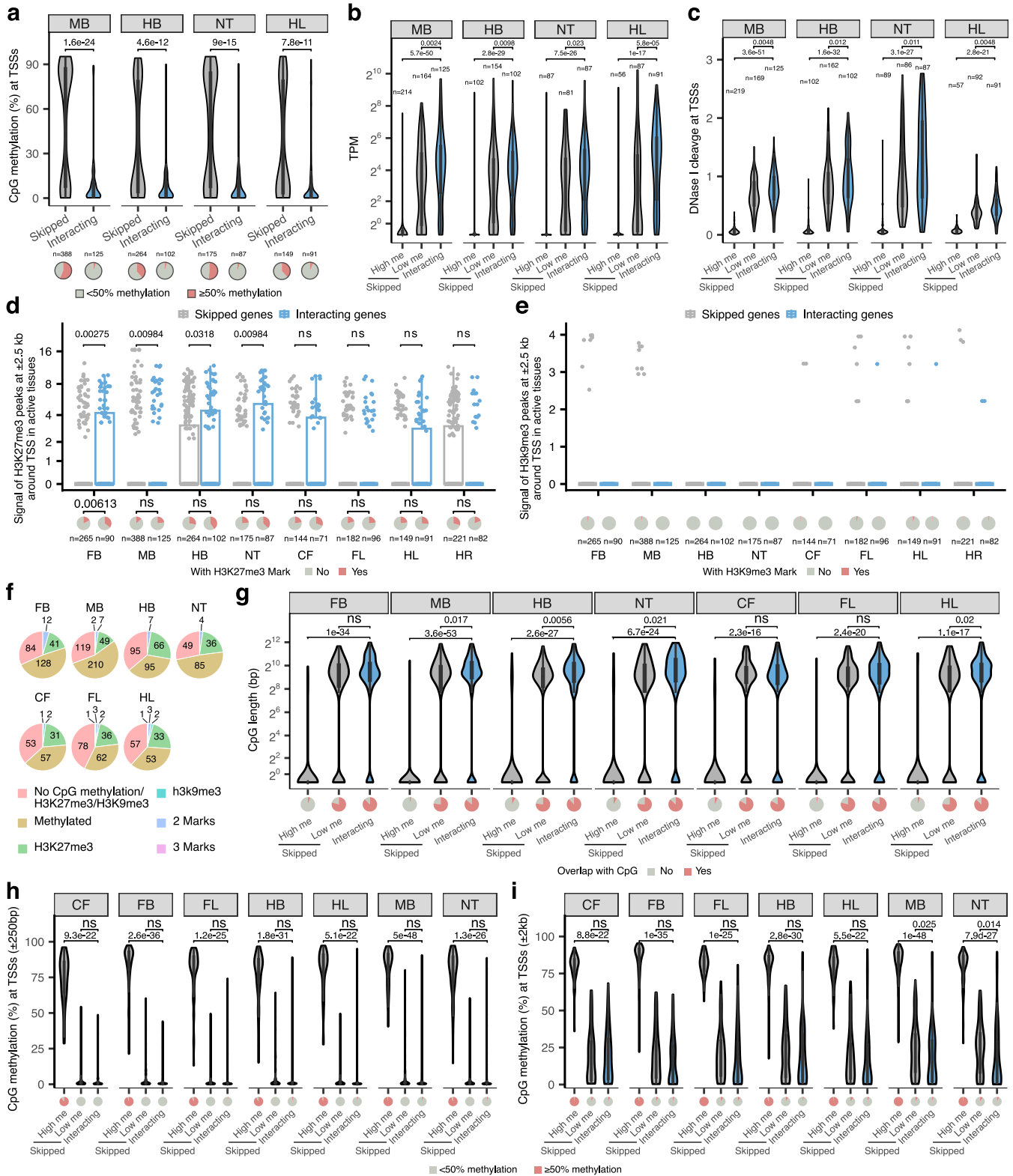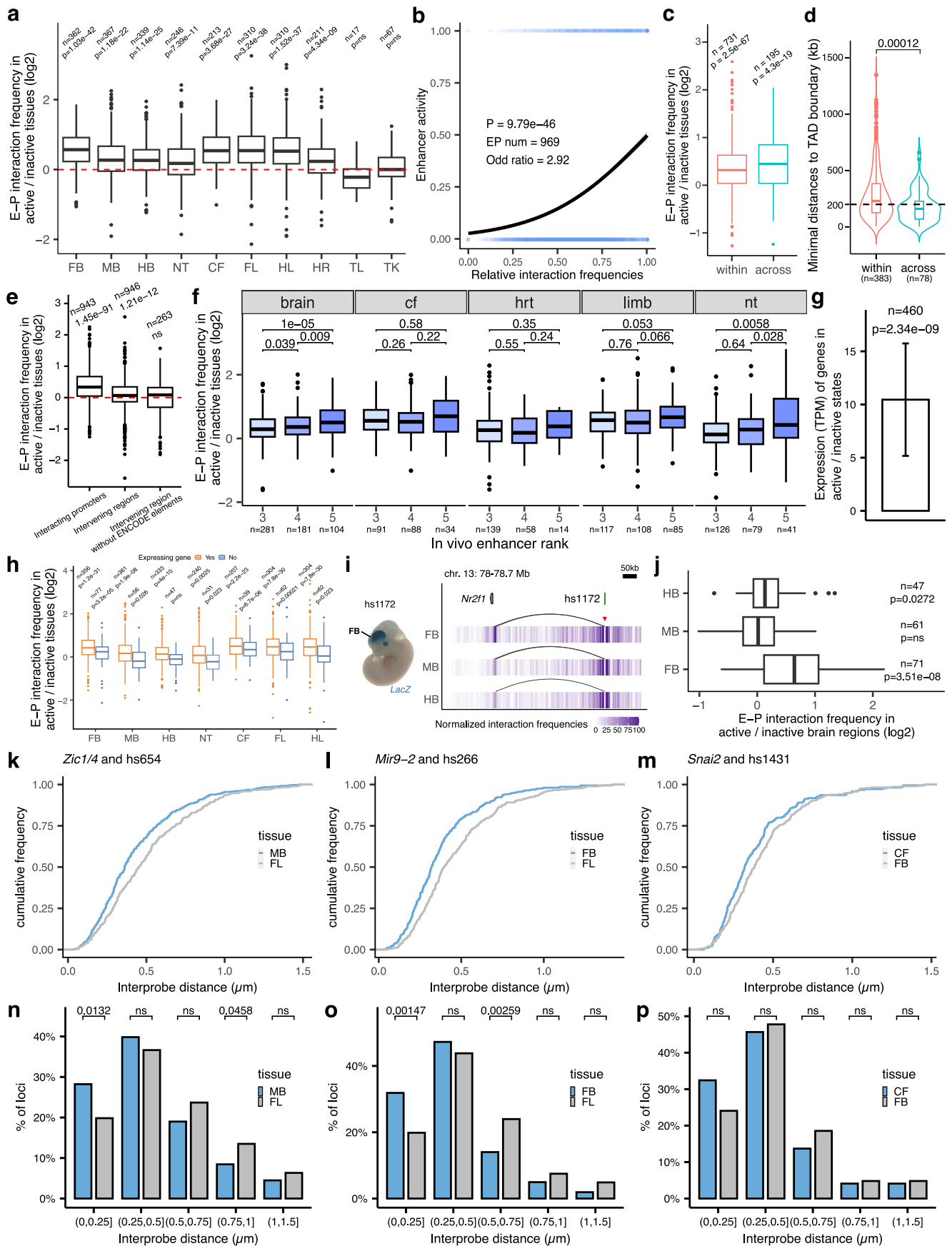
Extended Data Fig. 4 | See next page for caption.

Extended Data Fig. 4 | Properties of enhancer-interacting and skipped promoters. a–c, The CpG methylation (a), mRNA expression levels (b) and DNase signal (c) of enhancer-interacting and skipped promoters in tissues where enhancers are active. High me, high methylation skipped promoters (>50% CpG methylation within ±1 kb from TSS). Low me, low methylation skipped promoters (<50% CpG methylation within ±1 kb from TSS). **d, e**, H3K27me3 (d), H3K9me3 (e) signal at ± 2.5 kb of enhancer-interacting and skipped promoters in tissues where enhancers are active. The pie charts below show the fraction of promoters marked with H3K27me3 or H3K9me3. **f**, Pie charts showing the fraction of skipped promoters marked by CpG methylation, H3K27me3, H3K9me3 or the combination of marks. **g-i**, Violin plot showing CpG length (g), or CpG methylation level at transcription start sites for enhancer-interacting and skipped genes with different window sizes ± 250 bp (h) and ± 2 kb (i)). The number of high and low methylated skipped as well as interacting promoters

in CpG analysis are n = 58, n = 86 and n = 71 (CF), n = 138, n = 126 and n = 90 (FB), n = 64, n = 116 and n = 96 (FL) and n = 100, n = 162 and n = 102 (HB), n = 55, n = 92 and n = 91 (HL), n = 213, n = 169 and n = 125 (MB) and, n = 87, n = 86 and n = 87 (NT). FB, forebrain. MB, midbrain. HB, hindbrain. CF, face. FL, forelimb. HL, hindlimb. NT, neural tube. HR, heart. P values are calculated by two-sided Wilcoxon rank test after adjusted for multiple testing (a-c, f-i) or by one-sided chi-squared test (d, e). A statistical test was not performed for H3K9me3 since most of the values are zero. The same DNA methylation, mRNA expression, DNaseI hypersensitivity, H3K27ac and H3K9me3 dataset (a mixture of fore- and hindlimb buds) were used for both fore- and hindlimb interaction analyses. For the boxplots in panels a-e and g-i, the central horizontal lines are the median, with the boxes extending from the 25th to the 75th percentiles. The whiskers further extend by ±1.5 times the interquartile range from the limits of each box.

Enhancer	Viability: Results from Heterozygous Female x Heterozygous Male Matings					
	Pups Genotyped	+/+	+/-	-/-	chi-square	P-value
hs654	34	7	22	5	3.18	0.204
hs267-853	23	4	14	5	1.17	0.556

Extended Data Fig. 5 | *Zic1/Zic4* and *Mir9-2* brain enhancer knock-outs. a, Map of the deleted region encompassing hs654 midbrain enhancer of *Zic1/Zic4* together with H3K27ac, DNase-seq, ATAC-seq from midbrain and conservation track across 60 species. **b**, Sanger sequencing of the PCR product from hs654 knock-out mice (n = 4 biological replicates). **c**, representative PCR genotyping results of the hs654 enhancer knockout mice. Lanes in the gel were rearranged so that results for wild-type and heterozygous mice are adjacent to each other. **d**, Map of the deleted region encompassing hs267, hs266 and hs853 forebrain enhancers of *Mir9-2* together with H3K27ac, DNase-seq, ATAC-seq from midbrain and conservation track across 60 species. **e**, Sanger sequencing of the PCR product from hs267-853 knock-out mice (n = 3 biological replicates). **f**, representative PCR genotyping results of the hs267-853 enhancer knockout mice. **g**, Genotype frequency data for enhancer knockout lines. Mice homozygous for either deletion were born at normal Mendelian ratios, and no gross phenotypes or impairments were observed. P-values were calculated using the one-sided chi-square test.
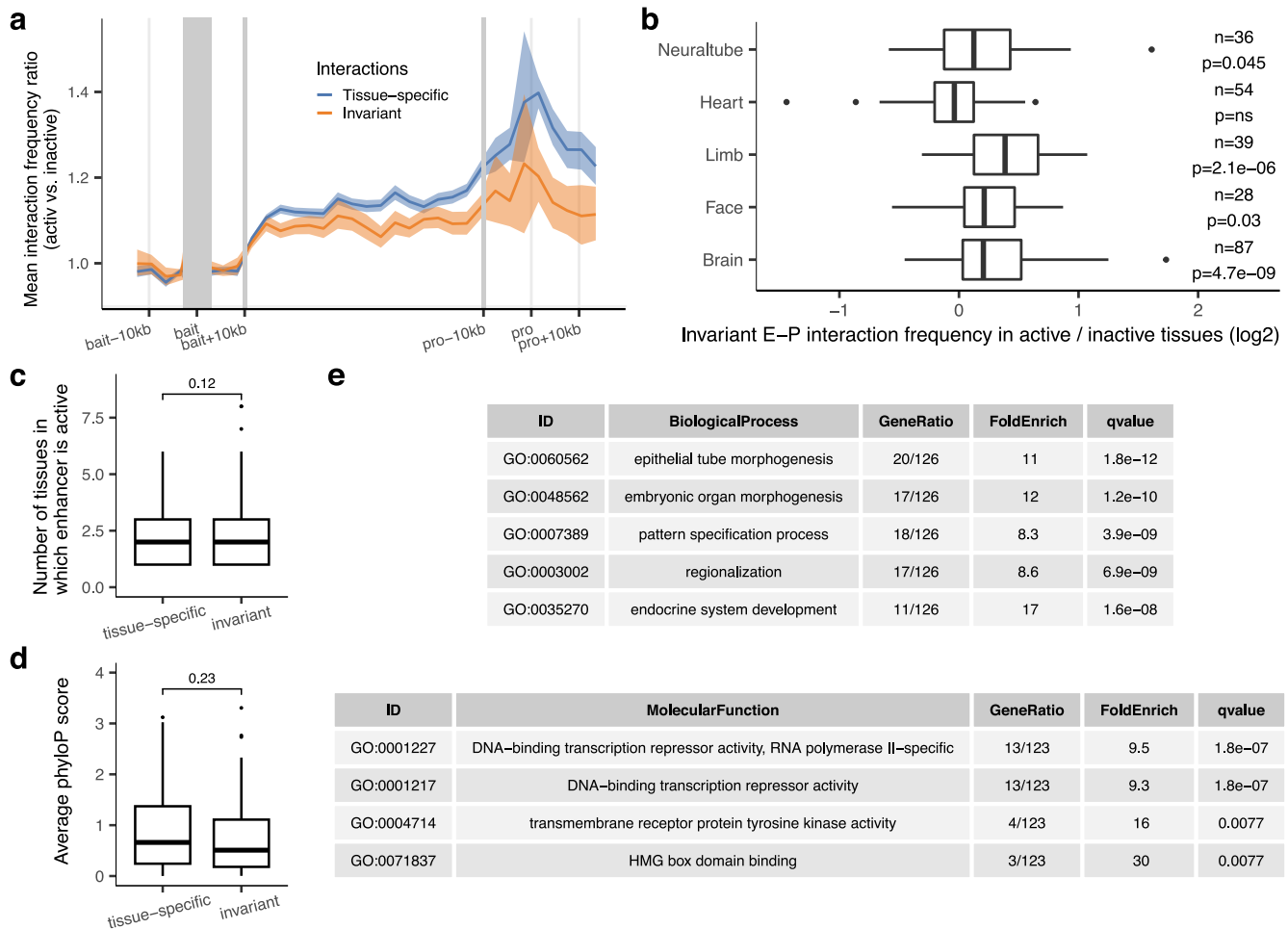
Extended Data Fig. 6 | Enhancer–promoter interaction frequency across tissues. a, The ratio of E–P interaction frequency between active and inactive tissues. Red dashed line indicates no difference between active and inactive tissues. **b**, Univariate logistic regression for relative interaction frequencies and enhancer activity across all tissues. **c**, The ratio of E–P interaction frequency between active and inactive tissues for interactions within or across TADs. **d**, The distribution of distances between the closest TAD boundary and enhancer for enhancers acting within or across TADs. **e**, The ratio of interaction frequency between active and inactive tissues on interacting promoters or intervening regions before and after removing ENCODE annotated elements (± 20 kb). Red dashed line indicates no difference between active and inactive tissues. **f**, The ratio of E–P interaction frequency between active and inactive tissues for enhancers with different ranks. Only tissues with ≥10 interactions in each rank category are shown. **g**, The fold-change of gene expression levels between active state (baited enhancers interact with active promoters) and inactive state (baited enhancers don't interact with promoters or in inactive tissues).

Data are represented as mean ± s.e.m. **h**, The ratio of E–P interaction frequency between active and inactive tissues for expressed genes (TPM > = 0.5) and lowly expressed or inactive genes (TPM < 0.5). **i**, Chromatin interaction profiles in forebrain, midbrain and hindbrain centered on the enhancer hs1172 at *Nr2f1* locus (chr13:78,057,768-78,705,499). **j**, The ratio of E–P interaction frequency between active and inactive brain regions for enhancers active in one of the brain domains. **k-m**, Cumulative frequency plots of interprobe distances for the indicated loci and tissues. n-p, Frequency distribution of FISH interprobe distances in 250 nm bins between *Zic1/4* and hs654 (**n**), *Mir9-2* and hs266 (**o**), *Snai2* and hs1431 (**p**) in indicated tissues. P values are calculated by paired-sample (a, c, e, g, h, j) or unpaired-sample (d, f) two-sided Wilcoxon rank test and adjusted for multiple testing or by one-sided chi-squared test (b, n-p). For the boxplots in panels a, c-f, h and j, the central horizontal lines are the median, with the boxes extending from the 25th to the 75th percentiles. The whiskers further extend by ±1.5 times the interquartile range from the limits of each box.

a

b

c

d

e

ID	BiologicalProcess	GeneRatio	FoldEnrich	qvalue
GO:0060562	epithelial tube morphogenesis	20/126	11	1.8e−12
GO:0048562	embryonic organ morphogenesis	17/126	12	1.2e−10
GO:0007389	pattern specification process	18/126	8.3	3.9e−09
GO:0003002	regionalization	17/126	8.6	6.9e−09
GO:0035270	endocrine system development	11/126	17	1.6e−08

ID	MolecularFunction	GeneRatio	FoldEnrich	qvalue
GO:0001227	DNA−binding transcription repressor activity, RNA polymerase II−specific	13/123	9.5	1.8e−07
GO:0001217	DNA−binding transcription repressor activity	13/123	9.3	1.8e−07
GO:0004714	transmembrane receptor protein tyrosine kinase activity	4/123	16	0.0077
GO:0071837	HMG box domain binding	3/123	30	0.0077

**Extended Data Fig. 7 | Properties of invariant enhancer–promoter interactions. a**, Metaplot showing average ratio of enhancer interaction frequency between active and inactive tissues for invariant (interactions present in all 7 main tissues: brain, face, limb, heart, neural tube, trunk and tail, n = 171) and tissue-specific (≤ 6 main tissues, n = 775) interactions. Light blue/orange shading indicates 95% confidence intervals estimated by non-parametric bootstrapping. 10 kb upstream and downstream of enhancer bait and target promoter are also indicated (grey bar). **b**, The average ratio of invariant enhancer-promoter interaction frequency between active and inactive tissues for enhancers active in the brain, face, limb, heart and neural tube E–P. Data is shown only for tissues with at least 20 active enhancers that form invariant E–P interactions. P values were calculated by paired-sample two-sided Wilcox test

and adjusted for multiple testing. **c**, The number of tissues in which enhancers forming invariant (10 tissues, n = 98) or tissue-specific (≤ 4 tissues, n = 196) E–P interactions are active in vivo. **d**, The average phyloP scores of enhancers forming invariant (10 tissues, n = 98) or tissue-specific (≤ 4 tissues, n = 196) E–P interactions. P values in panels c and d were calculated by two-sided Wilcox test. **e**, Gene Ontology enrichment for genes that form invariant (10 tissues) E–P interactions (Biological process and Molecular function). Q values were calculated by over-representation test and adjusted for multiple testing. For the boxplots in panels b-d, the central horizontal lines are the median, with the boxes extending from the 25th to the 75th percentiles. The whiskers further extend by ±1.5 times the interquartile range from the limits of each box.
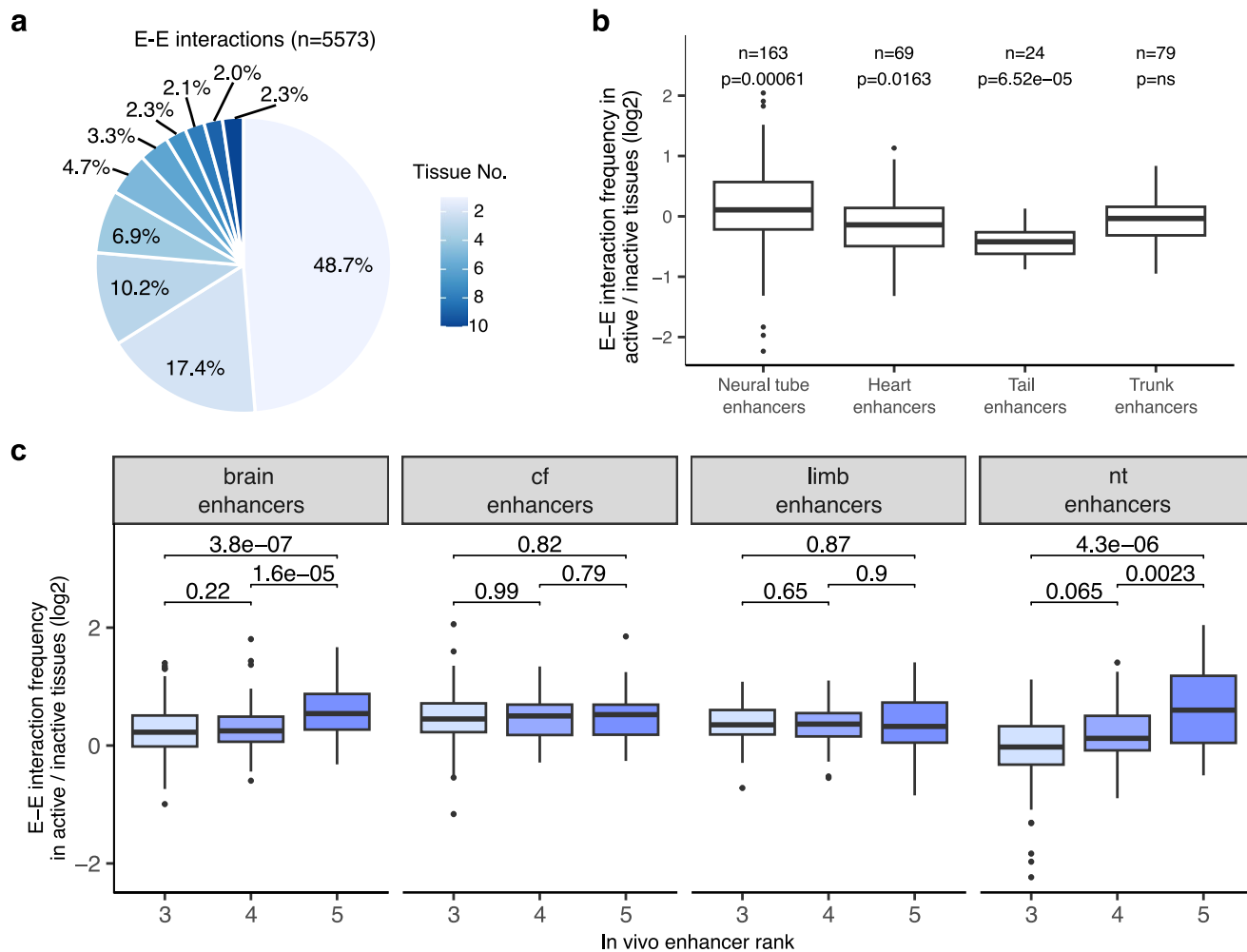
Extended Data Fig. 8 | Tissue specificity of enhancer-enhancer chromatin interactions. a, Pie chart showing the fraction of E–E interactions present in different numbers of tissues. **b**, The average ratio of E–E interaction frequency between active and inactive tissues for enhancers active in neural tube, heart, tail and trunk. The number of E–E interactions for each tissue is indicated at the top. P values were calculated by paired-sample two-sided Wilcox test and adjusted for multiple testing. **c**, The average ratio of enhancer–enhancer interaction frequency between active and inactive tissues for enhancers of different ranks.

The E–E interaction number for rank 3 to 5 are n = 217, n = 122 and n = 69 (brain), n = 53, n = 59 and n = 18 (cf), n = 100, n = 84 and n = 45 (limb), n = 80, n = 51 and n = 32 (nt), respectively. Cf: face. Nt: neural tube. P values were calculated by unpaired-sample two-sided Wilcox test with multiple testing. For the boxplots in panels b and c, the central horizontal lines are the median, with the boxes extending from the 25th to the 75th percentiles. The whiskers further extend by ±1.5 times the interquartile range from the limits of each box.
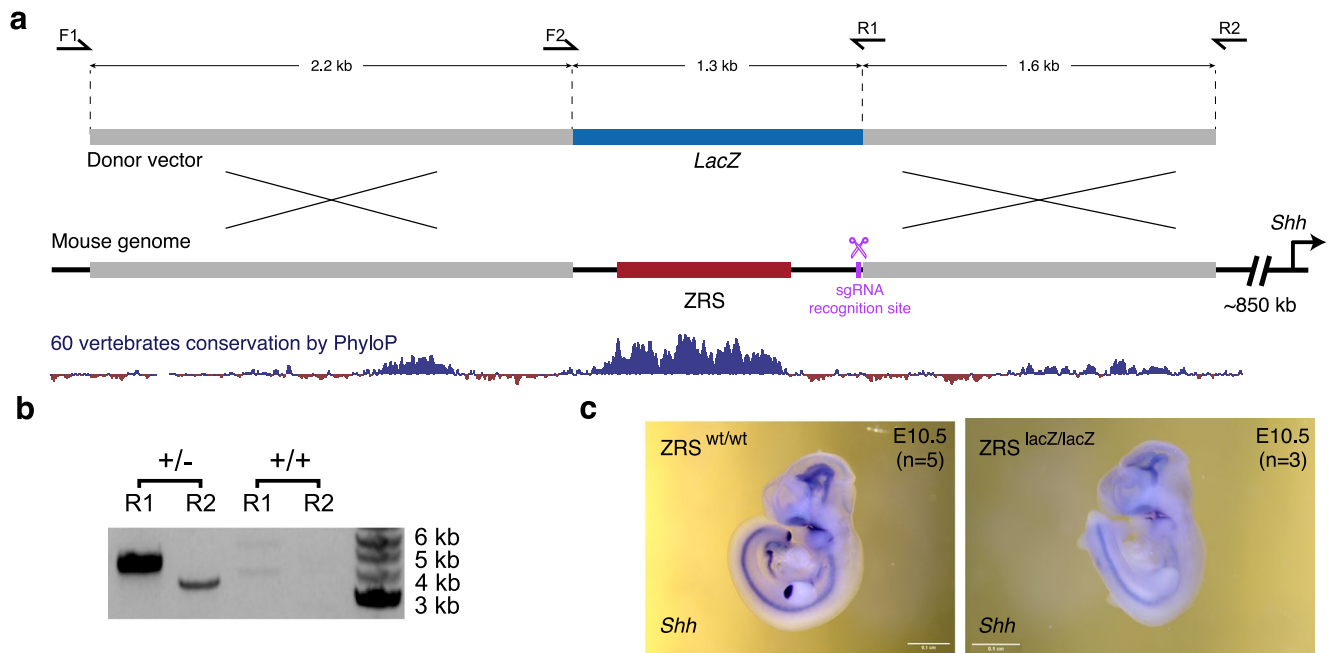
Extended Data Fig. 9 | CRISPR/Cas9-mediated ZRS limb enhancer replacement with a fragment of the lacZ gene. a, Schematic overview of the strategy for ZRS enhancer replacement. A 4.5 kb mouse genomic region containing the ZRS enhancer (red) is shown together with the vertebrate conservation track (dark blue). The donor vector contained two homology arms (gray) and an inactive fragment of the lacZ coding sequence (blue). The sgRNA recognition site is indicated in purple. PCR primers used for genotyping are shown as arrows. **b,** PCR genotyping analysis of heterozygous and wildtype mice using primer pairs LacZ-F1 and LacZ-R1 or LacZ-F2 and LacZ-R2. See Methods for details. **c,** Shh whole-mount in situ hybridization in E10.5 wild type (left) and ZRS^lacZ/lacZ knock-in embryos (n ≥ 3 biological replicates for each genotype). Shh expression is not detectable in limb buds but is present elsewhere in the embryo.

nature portfolio

Corresponding author(s): Evgeny Kvon

Last updated by author(s): Jan 24, 2024

Reporting Summary

Nature Portfolio wishes to improve the reproducibility of the work that we publish. This form provides structure for consistency and transparency in reporting. For further information on Nature Portfolio policies, see our Editorial Policies and the Editorial Policy Checklist.

Statistics

For all statistical analyses, confirm that the following items are present in the figure legend, table legend, main text, or Methods section.

n/a	Confirmed	
☐	☒	The exact sample size (*n*) for each experimental group/condition, given as a discrete number and unit of measurement
☐	☒	A statement on whether measurements were taken from distinct samples or whether the same sample was measured repeatedly
☐	☒	The statistical test(s) used AND whether they are one- or two-sided *Only common tests should be described solely by name; describe more complex techniques in the Methods section.*
☒	☐	A description of all covariates tested
☐	☒	A description of any assumptions or corrections, such as tests of normality and adjustment for multiple comparisons
☐	☒	A full description of the statistical parameters including central tendency (e.g. means) or other basic estimates (e.g. regression coefficient) AND variation (e.g. standard deviation) or associated estimates of uncertainty (e.g. confidence intervals)
☐	☒	For null hypothesis testing, the test statistic (e.g. F, t, r) with confidence intervals, effect sizes, degrees of freedom and P value noted *Give P values as exact values whenever suitable.*
☒	☐	For Bayesian analysis, information on the choice of priors and Markov chain Monte Carlo settings
☒	☐	For hierarchical and complex designs, identification of the appropriate level for tests and full reporting of outcomes
☒	☐	Estimates of effect sizes (e.g. Cohen's *d*, Pearson's *r*), indicating how they were calculated

Our web collection on statistics for biologists contains articles on many of the points above.

Software and code

Policy information about availability of computer code

Data collection	3D DNA-FISH images were taken by ZEISS LSM 900 Airyscan 2 .
Data analysis	Custom algorithms or software was not developed for this research. Data processing was performed using FastQC (v. >0.11.9), HiCUP (v. >0.8.0), STAR (v. >2.7.9a). Data analysis was primarily performed in R (v. >4.1.2) using a variety of published packages: CHiCAGO (v. >1.26.0), Chicdiff (v. 0.6), DEseq2 (v. >3.16), clusterProfiler (v. >3.0.4). 3D DNA-FISH images were analyzed with Imaris.

For manuscripts utilizing custom algorithms or software that are central to the research but not yet described in published literature, software must be made available to editors and reviewers. We strongly encourage code deposition in a community repository (e.g. GitHub). See the Nature Portfolio guidelines for submitting code & software for further information.

Data

Policy information about availability of data

All manuscripts must include a data availability statement. This statement should provide the following information, where applicable:
- Accession codes, unique identifiers, or web links for publicly available datasets
- A description of any restrictions on data availability
- For clinical datasets or third party data, please ensure that the statement adheres to our policy

Sequencing data generated in this study are available at the Gene Expression Omnibus repository with the accession number GSE217078. Several embryonic ChIP-seq / DNase-seq / bisulfite-seq / RNA-seq data for different tissues at E11.5 were downloaded from ENCODE (https://www.encodeproject.org/). The CTCF ChIP-seq

Human research participants

Policy information about studies involving human research participants and Sex and Gender in Research.

Reporting on sex and gender	N/A
Population characteristics	N/A
Recruitment	N/A
Ethics oversight	N/A

Note that full information on the approval of the study protocol must also be provided in the manuscript.

Field-specific reporting

Please select the one below that is the best fit for your research. If you are not sure, read the appropriate sections before making your selection.

☒ Life sciences   ☐ Behavioural & social sciences   ☐ Ecological, evolutionary & environmental sciences

For a reference copy of the document with all sections, see nature.com/documents/nr-reporting-summary-flat.pdf

Life sciences study design

All studies must disclose on these points even when the disclosure is negative.

Sample size	No prior analyses were used to determine the sample size before the experiment.
Data exclusions	The embryos that were not at the correct developmental stage were excluded from data collection. For DNA-FISH image analysis only alleles within the DAPI-stained area and with single probe signals were analyzed to eliminate sister chromatids. Inter-probe distances were measured with the closest distance between a pair of probes and only distances <1.5 µm were considered.
Replication	All capture Hi-C, RNA-seq and 3D FISH experiments were performed in least two biological replicates, each replicate includes the same tissue from multiple embryos with same genotype.
Randomization	For capture Hi-C and RNA-seq experiment, wild-type and knockin/knockout littermates were randomized and identified only by numbers with genotype unknown to the investigator during data collection and sample processing. For each tissue and corresponding probe set for DNA-FISH, random x-y coordinates were selected and a 9x9 tiled image was taken.
Blinding	For RNA-seq, investigators were blinded to animals' genotypes during sample collection and library preparation for two knockout lines generated in this study. For ISH experiments in knockin embryos, investigators were blinded to animals' genotypes during tissue collection and in situ hybridization. For capture Hi-C experiments blinding was not performed because all metrics were derived from absolute quantitative measurements without human subjectivity. For DNA-FISH, after manual data exclusions (see above) foci recognition and distance measurement was done by an automated algorithm (IMARIS).

Reporting for specific materials, systems and methods

We require information from authors about some types of materials, experimental systems and methods used in many studies. Here, indicate whether each material, system or method listed is relevant to your study. If you are not sure if a list item applies to your research, read the appropriate section before selecting a response.

Materials & experimental systems

n/a	Involved in the study
☒	☐ Antibodies
☒	☐ Eukaryotic cell lines
☒	☐ Palaeontology and archaeology
☐	☒ Animals and other organisms
☒	☐ Clinical data
☒	☐ Dual use research of concern

Methods

n/a	Involved in the study
☒	☐ ChIP-seq
☒	☐ Flow cytometry
☒	☐ MRI-based neuroimaging

Animals and other research organisms

Policy information about [studies involving animals](#); [ARRIVE guidelines](#) recommended for reporting animal research, and [Sex and Gender in Research](#)

Laboratory animals	All animals used in this study were of Mus musculus species and FVB/NCrl strain and were assayed at embryonic days 10.5 and 11.5.
Wild animals	The study did not involve wild animals.
Reporting on sex	Sex was not determined for embryo collection, but cohorts were presumed to include roughly equal numbers of males and females.
Field-collected samples	The study did not involve samples collected from the field.
Ethics oversight	All animal work was reviewed and approved by the Lawrence Berkeley National Laboratory Animal Welfare and Research Committee and the University California Irvine Laboratory Animal Resources (ULAR).

Note that full information on the approval of the study protocol must also be provided in the manuscript.